

*Optimising the characterisation of quantum
processes*

A DISSERTATION PRESENTED

BY

JAKE GULLIKSEN

TO

THE PHYSICS AND ASTRONOMY DEPARTMENT

IN PARTIAL FULFILLMENT OF THE REQUIREMENTS

FOR THE DEGREE OF

DOCTOR OF PHILOSOPHY

IN THE SUBJECT OF

PHYSICS

AARHUS UNIVERSITY

DENMARK

APRIL 2014

© 2014 - *JAKE GULLIKSEN*
ALL RIGHTS RESERVED.

Optimising the characterisation of quantum processes

ABSTRACT

This thesis presents efficient strategies for characterising quantum processes and, more specifically, how that applies to characterising the gates used in quantum computation. The basics, promises, limitations and successes of quantum computation are summarized in chapter 1. In particular, quantum tomography is introduced as a means to evaluate the achievements of computational tasks. In chapter 2 we discuss tools to facilitate the simulation of quantum computing and provide the formalism for characterising quantum processes. Chapter 3 introduces neutral atoms as a potential route to large scale quantum computing and develops a numerical implementation based on Rydberg atoms and their interactions.

In chapter 4 we present an efficient method to simulate a quantum process subject to dissipation and noise. To describe the effect on any input state we propagate Monte Carlo wave functions for a principal and ancilla system, initially prepared in an entangled state. In analogy to experimental process tomography, the simulated propagator for the system density matrix is conveniently described by the *process matrix* - directly determined from the stochastic state vectors. We show that the method significantly reduces the computational complexity compared with standard theoretical characterisation techniques. It also delivers an upper bound on the trace distance between the ideal and simulated process based on the evolution of only a single wave function of the entangled system. A proof-of-principle demonstration is performed using a Rydberg mediated controlled-Z gate.

In chapter 5 we study the achievements of quantum circuits comprised of several one- and two-qubit gates. Quantum process matrices are determined for the basic one- and two-qubit gate operations and concatenated to yield the process matrix of the combined quantum circuit. Examples are given of process matrices obtained by a Monte Carlo wave function analysis of Rydberg blockade gates in neutral atoms. Our analysis is ideally suited to compare different implementations of the same process. In particular, we show that the three-qubit Toffoli gate facilitated by the simultaneous interaction between all atoms may be accomplished with higher fidelity than a concatenation of one- and two-qubit gates. Chapter 6 concludes the thesis.

Contents

1	QUANTUM COMPUTATION	1
1.1	Bits and Qubits	2
1.2	Quantum gates	3
1.3	Quantum algorithms	4
1.4	Implementations	6
1.5	Quantum tomography	7
2	UNDERLYING CONCEPTS	9
2.1	Density operator	10
2.2	Master equation	12
2.3	Monte Carlo wave functions	14
2.4	Effective operator formalism	17
2.5	Process characterisation	19
2.6	Conclusion	23
3	RYDBERG ATOMS	24
3.1	Manipulating single atoms	25
3.2	Rydberg atoms and their interactions	26
3.3	Single-atom Hamiltonian	32
3.4	Effective single-atom Hamiltonian	36
3.5	Two-atom Hamiltonian	41
3.6	Conclusion	43

4	EFFICIENT PROCESS CHARACTERISATION	44
4.1	Process characterisation with Monte Carlo	45
4.2	Upper bound error estimate from a single trajectory	49
4.3	Rydberg mediated controlled-Z gate	50
4.4	Error analysis	56
4.5	Discussion and conclusion	56
5	ERROR ACCUMULATION IN QUANTUM CIRCUITS	59
5.1	Process matrix identification	61
5.2	The process matrix for a quantum circuit	62
5.3	Rydberg blockade quantum gates	65
5.4	The Toffoli gate by Rydberg blockade	68
5.5	Conclusion	71
6	CONCLUSION AND FUTURE DEVELOPMENT	73
	REFERENCES	83

Preface

It has been a privilege to spend the last three years studying at the University of Aarhus. This thesis records the work carried out at the department of physics and astronomy under the supervision of Klaus Mølmer. Just a few points on style: I use the convention that $\hbar = 1$, which means that the terms energy and frequency are used interchangeably. To avoid clutter, the hats typically donning operators have been neglected, as I feel it will not confuse the reader.

At the top of the thank you list is my supervisor, Klaus Mølmer. Your aptitude for creative and intuitive ideas is truly amazing. It worked out quite well, because I had plenty of questions and you always had plenty of answers. I am also very grateful to Durga Dasari who has been my unofficial supervisor and is always ready to nut out a problem with me. He was also of great help in the proof reading process. During the course of my study here we have been collaborating with the group in Madison and I thank Mark Saffman for his help with everything experimental. Thanks to Malte Tichy who proof read this thesis, you certainly have a knack of making a sentence get to the point. All the guys on the sixth floor of the big yellow building have been great, its been a pleasure getting to know you (and often your significant other). Notable mentions go out to Maciek and Steve, who have been the reason behind long coffee breaks while discussing, well, physics and everything. On a more serious note, I thank the Lord for guiding me through the last three years. My family have been very supportive, once they even tried to read some of my work. They said the pictures looked nice. At the bottom of the list,

but it isn't a list of decreasing importance, is my wife Beccy. Thank you for coming with me to Denmark, leaving family far behind. You have been very encouraging, and I really appreciated your patience when I needed to study for "one more hour".

In natural science, Nature has given us a world and we're just to discover its laws. In computers, we can stuff laws into it and create a world.

Michael Rabin

1

Quantum computation

In essence, the Church-Turing principle states that: Given a finite amount of time, a human armed with enough paper and pens could, in principal, compute any function that is algorithmically computable. Without getting into the details of this principle, which are still under discussion, we go to 1985 when David Deutsch made an interesting reformulation of the Church-Turing principle. It went as follows [1]: *Every physical process can be simulated by a universal computer.* This phrasing recognizes that computation is simply a physical process. Input information is stored on a physical system, the processing is through some physical means, and output is, again, stored on a physical system. Given physical processes are fundamentally quantum mechanical, Deutsch proposed that his “universal computer” could be operated at the quantum level, using algorithms exploiting properties unique to quantum mechanics. Applied to the simulation of quantum systems [2], for example, *quantum computation* would have exponential speed-up over classical

methods. Quantum computers do not negate the validity of the Church-Turing principle but, in some cases, they would significantly reduce the time that humans spend with their pencils. However, this all remained largely speculative until 1994 when Shor introduced his quantum factoring algorithm [3, 4].

1.1 BITS AND QUBITS

Classical bits, termed 0 and 1, are distinct states stored on some physical system. In modern day computers this usually means differences in electrical voltage or current pulses. However, there is no reason why this information cannot be stored as states on a quantum system. These quantum bits, or qubits, may exist in any superposition of the quantum states $|0\rangle$ and $|1\rangle$, taking the form

$$|\psi\rangle = c_0|0\rangle + c_1|1\rangle, \quad (1.1)$$

a property arising from the linearity of the Hilbert space. A measurement on an ensemble of two-state quantum systems will find the outcomes $|0\rangle$ or $|1\rangle$ with a frequency $|c_0|^2$ and $|c_1|^2$, respectively. Because the measurements reveal a set of probabilities, it follows that the coefficients satisfy the normalization condition $|c_0|^2 + |c_1|^2 = 1$.

In classical computer architecture, a processor register is the storage of a small number of bits. By extension of Eq. (1.1) its quantum analogue, the n -qubit register, may be in any superposition of the 2^n basis states

$$|\Psi\rangle = \sum_{x_1=0}^1 \sum_{x_2=0}^1 \cdots \sum_{x_n=0}^1 c_{x_1 x_2 \dots x_n} |x_1\rangle |x_2\rangle \cdots |x_n\rangle. \quad (1.2)$$

An important feature distinguishing the qubit from its classical counterpart is that multiple qubits may exhibit quantum entanglement. This is exemplified in the Bell state

$$|\Psi\rangle = \frac{|00\rangle + |11\rangle}{\sqrt{2}}. \quad (1.3)$$

(a)	Input	Output
	0 0	0
	0 1	0
	1 0	0
	1 1	1

(b)	Input	Output
	0	1
	1	0

Figure 1.2.1: Truth tables for the logical (a) AND and (b) NOT gate

This state cannot be written as the product of two distinct qubit states. A measurement on either qubit will produce the state $|0\rangle$ or $|1\rangle$, each with a probability of 50%, but, after measurement on the first qubit, the state of the second qubit will inevitably be the state of the first. That is, these qubits are maximally entangled, or said to be perfectly correlated. Entanglement allows multiple states to be acted on simultaneously and is considered a resource, unique to quantum computing (but see Ref. [5] where the “amount” of entanglement is shown not to determine the success or failure of quantum computation).

1.2 QUANTUM GATES

In 1973 there was a remarkable discovery in classical computing. It was found that all computational tasks can be reduced down into a series of gates, each of which are logically reversible [6]. At the time, reversible gates solved the unavoidable problem of heat generation caused by discarding information [7]. To see how information is lost in an ordinary classical gate we consider the AND gate (Fig. 1.2.1(a)). If the output is 0, the input could be any one of 00, 01 and 11, there is no way to identify the original signal. On the other hand the NOT gate, defined by the truth table in Fig. 1.2.1(b), is reversible. Unfortunately, the NOT gate is not enough for “universal” computing, that is, it is not able to perform every logical operation. A solution for universal, reversible computing was found in the three-bit Toffoli gate [8], it became apparent, however, that the price for reversibility was the inclusion of idle bits.

To see how this discussion is important for quantum computation we remember that the laws of quantum physics are reversible in time. If Schrödinger's equation describes the evolution of a qubit through a gate then that gate is necessarily reversible. A few frequently seen examples of single qubit gates are the NOT (X), Hadamard (H) and $\pi/8$ phase shift (T) gates. Gates may be expressed as unitary matrices and qubits as column vectors in \mathbb{C}^2 . In the single qubit computational basis $\{|0\rangle, |1\rangle\}$ these gates are represented by

$$X = \begin{pmatrix} 0 & 1 \\ 1 & 0 \end{pmatrix}, \quad H = \frac{1}{\sqrt{2}} \begin{pmatrix} 1 & 1 \\ 1 & -1 \end{pmatrix} \quad \text{and} \quad T = \begin{pmatrix} 1 & 0 \\ 0 & e^{i\pi/4} \end{pmatrix}. \quad (1.4)$$

The fact that the T gate has no factor of $\pi/8$ is a historical curiosity but it may be returned by multiplying the gate with the global phase factor $e^{-i\pi/8}$.

Unlike classical logic operations, there is no single “universal” quantum gate. However, the Hadamard and $\pi/8$ gates together with the two-qubit CNOT gate constitute one universal *set* of quantum gates. The CNOT, or controlled-NOT, gate performs a NOT operation on the second (target) qubit if and only if the state of the first (control) qubit is $|1\rangle$. It is represented by the unitary

$$U_{\text{CNOT}} = \begin{pmatrix} 1 & 0 & 0 & 0 \\ 0 & 1 & 0 & 0 \\ 0 & 0 & 0 & 1 \\ 0 & 0 & 1 & 0 \end{pmatrix}, \quad (1.5)$$

in the two-qubit computational basis $\{|00\rangle, |01\rangle, |10\rangle, |11\rangle\}$. Any quantum logic operation may be simulated to an arbitrary degree of precision using the universal set of quantum gates.

1.3 QUANTUM ALGORITHMS

Simply put, quantum algorithms are algorithms that may only be carried out efficiently on a quantum computer. The first quantum algorithm was found in 1985

[1] and more followed, promising to efficiently solve problems that were seemingly infeasible using classical methods. A well cited use for this ability is breaking current cryptography codes. However, it also holds fundamental appeal by asking “Can quantum algorithms be used to solve all problems that are classically intractable?”. Presently, all quantum algorithms fall under three categories: The Abelian hidden subgroup problem, those based on amplitude amplification and simulation of quantum mechanical systems. In this section we will give the flavour of each, but for details refer to [9].

The most recognized example under the class of Abelian hidden subgroup problems is Shor’s factoring algorithm [3, 4], which can factor a number exponentially faster than the best classical algorithm, the number field sieve [10]. The difficulty of factoring is at the heart of current public-key cryptography. For instance, the RSA encryption scheme depends on the classically intractable problem of finding prime factors from a large composite number [11]. A successful realization of Shor’s factoring algorithm would render RSA obsolete. This class also incorporates many of the early quantum algorithms, such as those solving the more artificial problems posed by Deutch-Jozsa [12] and Simon [13].

The class of algorithms based on amplitude amplification is best exemplified by the Grover search algorithm [14] which offers quadratic speed up over classical approaches. Suppose we are searching for one item in an unsorted database of N items. There is no clever classical algorithm that succeeds with an average better than $N/2$ queries. Grover’s algorithm is a sequence of unitary operations that finds, with near certainty, the correct answer in $(\pi/4)\sqrt{N}$ steps. It does not offer exponential speed-up like Shor’s algorithm but has significant advantage over classical approaches for large N . Furthermore, Grover’s algorithm is optimal, in the sense that no other quantum search algorithm can do better than order $\mathcal{O}(\sqrt{N})$.

The simulation of quantum mechanical systems was predicted by Feynman to be a useful application of quantum computers [2]. The memory requirements for a computer to hold the coefficients of N quantum states grows exponentially with N . A natural solution would be to simulate quantum systems using quantum simulators. Toward this end, Feynman’s idea was to discretize time and space. The

finer details of designing Hamiltonians that would emulate the desired quantum properties came later with Lloyd [15] and Zalka [16]. The grand goal was to find “a quantum machine that could imitate any quantum system, including the physical world” [2], realistically, a means to study few-body correlations or densities would be enough.

1.4 IMPLEMENTATIONS

For a physical system to be considered for quantum computation, it must isolate the qubits involved from the environment, which constantly “measures” the state of the qubit, thereby causing decoherence. The system must also facilitate strong interactions between qubits, necessary for fast two-qubit gates. Inevitably then, there is a trade-off for large-scale quantum computing between a strong qubit-qubit coupling and weak qubit-environment coupling.

Currently, there is no consensus regarding the best implementation for a quantum computer. However, DiVincenzo has devised a scale with which to measure the validity of each approach [17], his criteria are

- A scalable physical system with well characterised qubits
- A method to initialize the method to a known quantum state
- A qubit’s coherence time must exceed the gate’s operation time
- The implementation of a universal set of quantum gates
- The readout of computational results

Noteworthy implementations that have met varying degrees of success are trapped ions [18–20], neutral atoms [21–23], nuclear magnetic resonance [24, 25] and quantum dots [26]. The main difficulty encountered by these systems is avoiding the trade-off mentioned above. For a helpful review on the progress of these implementations see reference [27].

In general a quantum computer is designed to be robust against decoherence, but in the unavoidable event of error it is necessary to have a correction strategy. The key idea of error correction is to protect a message by adding redundant information [28, 29]. Usually this means encoding a single logical qubit with several physical qubits. That way, even if one of the physical qubits decoheres we will still be able to derive the appropriate information from the logical qubit. Perhaps not surprisingly, quantum error correction has many parallels with its classical counterpart.

1.5 QUANTUM TOMOGRAPHY

We prepare the state vector $|\psi\rangle$ (or density operator ρ), but how well has it been prepared? We subject the state to a non-unitary operation, but how do we design an optimal implementation and what is the resultant state? In the corresponding classical case these questions have easy answers. An observer can measure the particle and trajectory without disturbing them. However, quantum mechanics require us to take more care. The answer is the subject of quantum tomography. Quantum tomography can refer to two disciplines, *state* and *process* tomography. Because the latter makes use of the former we begin by introducing state tomography.

Quantum state tomography experimentally determines a mixed quantum state. It is not as straightforward as measuring the state because *any* observation will alter it, preventing a true characterisation. Instead, an indirect approach may be taken by making many measurements on the same state, systematically modifying the experimental apparatus so that we can build statistics associated with different bases. An analysis of the resultant data allows a reconstruction of the state's information that is tomographically complete. State tomography has reached a high level of sophistication in the interest of accuracy and efficiency, pushing forward to the characterisation of larger and larger states [30].

Quantum process tomography experimentally determines a quantum process. It has been demonstrated in NMR [31, 32], optical [33, 34] and atomic systems

[35]. To proceed, we prepare an ensemble of known input states and send them through the applicable process (a CNOT gate for example). The original proposal, standard quantum process tomography (SQPT) [36–38] requires an implementation on a number of input states that scales exponentially with the number of qubits. The process is characterised by measuring all output states via quantum *state* tomography. In the case of specified operations we can compare the (process tomographic) result against what we would expect from an unitary operation to determine the quality of the process’s experimental implementation.

Other techniques have been developed for characterising a quantum process. Ancilla-assisted quantum process tomography (AAPT) [39–42] encodes the information of all input states into a single maximally entangled system-ancilla state in a doubled Hilbert space. Also, while both SQPT and AAPT rely on state tomography of the output state, direct characterisation of quantum dynamics [43–45] directly addresses features of the underlying dynamics via suitable “probe” systems and corresponding measurements. For more details and an investigation of resource demands for each strategy see reference [46].

2

Underlying concepts

In this chapter we consider existing theory which provides a framework for later chapters and as such does not represent original research. The key theme throughout this thesis is the development of *efficient* methods to characterise quantum processes and much effort was spent on implementing numerical means to achieve this. The mathematical tools used to facilitate numerical efficiency will be introduced and discussed.

In section 2.1 we introduce the density operator which describes a state evolving in an open quantum system. Section 2.2 we discuss evolution of the density operator by summarising the master equation derivation. Here, we will also introduce the assumptions held in all future chapters. Section 2.3 explores an alternative route to the master equation based on the stochastic evolution of wave functions. In section 2.4 a set of effective Hamiltonian and “quantum jump” operators are introduced. These operators avoid the often tedious calculations as-

sociated with finding effective forms for processes with unwanted time-scales. In section 2.5 we discuss the formalism involved in characterising a quantum process. Section 2.6 concludes the chapter.

2.1 DENSITY OPERATOR

If a system in the Schrödinger picture is prepared in the state $|\psi\rangle$ then we may define the density operator by the outer product

$$\rho = |\psi\rangle\langle\psi|. \quad (2.1)$$

Thus, if we specify a state $|v\rangle$, the integral $\langle v|\rho|v\rangle$ is the probability of finding the system in the state $|v\rangle$. The quantum state described by a *single* state vector is referred to as a pure state and contains the most information that can be known about a system. In reality, it is infeasible to have complete information about the system and we are required to perform statistical averages in order to describe quantum observables. These statistical mixtures, made up from an ensemble of states, are called mixed states and examples include an ensemble at thermal equilibrium or a mixture of independently prepared states.

Suppose that we have an ensemble of state vectors, $\{|\psi^{(1)}\rangle, |\psi^{(2)}\rangle, \dots, |\psi^{(n)}\rangle\}$, with the associated probability distribution $\{p_1, p_2, \dots, p_n\}$. This ensemble has both quantum probabilities inherent to each state vector and classical probabilities given by p_k . The density *operator* of a mixed state is defined by

$$\rho = \sum_{k=1}^n p_k |\psi^{(k)}\rangle\langle\psi^{(k)}|, \quad (2.2)$$

and the corresponding density *matrix* is

$$\rho_{ij} = \sum_{k=1}^n \langle i|\psi^{(k)}\rangle\langle\psi^{(k)}|j\rangle, \quad (2.3)$$

written in the (orthogonal) basis $\{|i\rangle\}$. As an example, consider an ensemble of n

wave functions $|\psi^{(k)}\rangle = \sum_i c_i^{(k)} |i\rangle$, Eq. (2.3) becomes

$$\rho_{ij} = \frac{1}{n} \sum_{k=1}^n p_k c_i^{(k)} c_j^{(k)*} = \overline{c_i c_j^*}. \quad (2.4)$$

We see that ρ_{ij} , the density matrix elements, are an average of the wave function ensemble's expansion coefficients.

Physical quantities are represented by linear operators, A , and the expectation value of any observable can be expressed in terms of ρ , that is,

$$\begin{aligned} \langle A \rangle &= \sum_{k=1}^n p_k \langle \psi^{(k)} | A | \psi^{(k)} \rangle \\ &= \sum_{ij} \sum_{k=1}^n p_k \langle \psi^{(k)} | i \rangle \langle i | A | j \rangle \langle j | \psi^{(k)} \rangle \\ &= \sum_i \sum_{k=1}^n p_k \langle i | \psi^{(k)} \rangle \langle \psi^{(k)} | A | i \rangle \\ &= \text{Tr}\{\rho A\}. \end{aligned} \quad (2.5)$$

Thus, all information about the mixed state is contained in the density operator of the state, whose elements by Eq. (2.4), can be expressed by an ensemble of wave functions.

2.1.1 DENSITY OPERATOR PROPERTIES AND PROPAGATION

As a point of reference, here are some properties of the density operator.

1. $\text{Tr}\{\rho\} = 1$, this can be seen from the definition of ρ in Eq. (2.2):

$$\text{Tr}\{\rho\} = \sum_k p_k \langle \psi^{(k)} | \psi^{(k)} \rangle = 1. \quad (2.6)$$

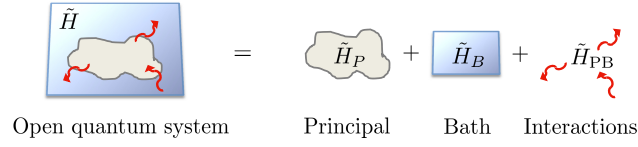


Figure 2.2.1: Hamiltonian of an open quantum system: To derive the master equation, the Hamiltonian of the entire system \tilde{H} is separated into the Hamiltonian for the principal system \tilde{H}_P and bath \tilde{H}_B together with the Hamiltonian for the interactions between them \tilde{H}_{PB} . The objective is find equations of motion solely for the principal system by removing all contributions of the bath.

2. The density operator ρ is positive semi-definite: For any state $|i\rangle$ we find

$$\langle i|\rho|i\rangle = \sum_k p_k |\langle i|\psi^{(k)}\rangle|^2 \geq 0. \quad (2.7)$$

Given the system Hamiltonian H , the equations of motion for the density operator have a direct correspondence to Schrödinger's equation for the evolution of states, that is,

$$\dot{\rho}(t) = -i[H, \rho(t)], \quad (2.8)$$

which is also known as Von Neumann's equation.

2.2 MASTER EQUATION

The implementation of a quantum gate protocol is not an isolated system. In this section we consider a formalism to simulate a principal system coupled to an environment (called the bath). We assume that the time evolution of the total principal plus bath system is unitary. The corresponding Hamiltonian $\tilde{H} = \tilde{H}_P + \tilde{H}_B + \tilde{H}_{PB}$ consists of the principal (P) and bath (B) Hamiltonians together with the Hamiltonian \tilde{H}_{PB} describing interaction between the principal and bath systems (Fig. 2.2.1). A straightforward solution for the evolution of the system-bath system is unhelpful as we are really only interested in deriving equations of motion

for the principal system. This is achieved by tracing out contributions of the bath, described below.

Evolution of the total density operator $\tilde{\rho}_T$ in the interaction picture is

$$\dot{\rho}_T(t) = -i[H_{PB}(t), \rho_T(t)], \quad (2.9)$$

where $\rho_T(t) = U^\dagger \tilde{\rho}_T U$, $H_{PB}(t) = U^\dagger \tilde{H}_{PB} U$ and $U = \exp\{-i(\tilde{H}_P + \tilde{H}_B)t\}$. The formal solution in a series of two iterations is

$$\begin{aligned} \rho_T(t) = & \rho_T(0) - i \int_0^t dt' [H_{PB}(t'), \rho_T(0)] \\ & - \int_0^t dt' \int_0^{t'} dt'' [H_{PB}(t'), [H_{PB}(t''), \rho_T(t'')]], \end{aligned} \quad (2.10)$$

which is the general expression for the operators evolution. We describe the evolution of the principle system under three assumptions. (1) *Born approximation*: Coupling between the principal and bath system is weak, that is, we proceed with Eq. (2.10), a solution accurate to second order in H_{PB} . This also implies that the bath's density operator ρ_B is not affected by the interaction. (2) *Product initial state*: Initially the principal system and bath are not correlated, that is, they may be written as the product state $\tilde{\rho}_T(0) = \tilde{\rho}_P(0) \otimes \tilde{\rho}_B(0)$. (3) *Markov approximation*: The correlation time between principal system and bath is very short. Differentiating Eq. (2.10) with respect to t and tracing over the bath variables, denoted by Tr_B , we find

$$\dot{\rho}_P(t) = - \int_0^\infty dt \text{Tr}_B \{ [H_{PB}(t), [H_{PB}(t - \tau), \rho_P(t) \otimes \rho_B]] \}, \quad (2.11)$$

where $\rho_P(t) = \text{Tr}_B\{\rho_T(t)\}$. From Eq. (2.11) a number of useful master equations may be derived.

The present master equation does not guarantee preservation of the density operator properties discussed in Sec. 2.1.1. It can be shown [47] that the master equa-

tion in Lindblad form

$$\dot{\rho}_P(t) = -i[H_P(t), \rho_P(t)] - \frac{1}{2} \sum_k (L_k^\dagger L_k \rho_P(t) + \rho_P(t) L_k^\dagger L_k) + \sum_k L_k \rho_P(t) L_k^\dagger, \quad (2.12)$$

conserves the positivity and normalization of the principal system's density operator $\rho_P(t)$. The Lindblad (L_k) operators, or decoherence operators, in Eq. (2.12) act in the space of the principal system. Thus, by solving Eq. (2.12) with the principal system's Hamiltonian H_P we determine the evolution of the principal system's state under the influence of damping and noise. In the following we refer to H and ρ as the principal system's Hamiltonian and density operator respectively.

2.3 MONTE CARLO WAVE FUNCTIONS

We may reproduce the predictions of the master equation (2.12) by introducing a stochastic element into the evolution of Monte Carlo wave functions [48–50]. These are wave functions, $|\psi(t)\rangle$, propagated with the non-Hermitian Hamiltonian $H_{\text{NH}} = H - i/2 \sum_k L_k^\dagger L_k$. Due to the non-unitary evolution during a small time step dt

$$|\psi_0(t + dt)\rangle = (1 - iH_{\text{NH}} dt) |\psi(t)\rangle, \quad (2.13)$$

the square of the norm associated with $|\psi_0(t + dt)\rangle$ is reduced by

$$\delta p = \sum_k \delta p_k = dt \sum_k \langle \psi(t) | L_k^\dagger L_k | \psi(t) \rangle. \quad (2.14)$$

The next step involves a random choice. Either the wave function $|\psi_0(t + dt)\rangle$ is re-normalized or, with probability δp , the wave function is subject to a quantum jump. This constitutes a collapse of the wave-function and with a branching ratio of $\delta p_k / \delta p$, the final state is chosen among the states $L_k |\psi(t)\rangle$. Thus, at time $t + dt$

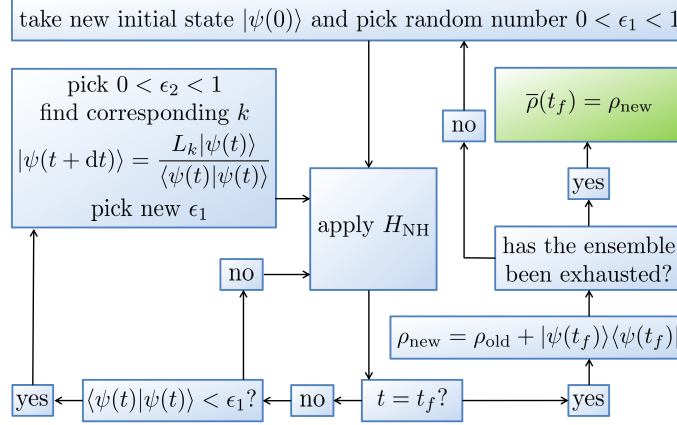


Figure 2.3.1: Simulation flowchart: Implementation of the Monte Carlo wave function method describing the evolution of a state from initial time $t = 0$ to final time $t = t_f$. The stochastic nature of the method requires use of the random numbers ϵ_1 and ϵ_2 which dictate the evolution of the wave function $|\psi(t)\rangle$. Each wave function in the ensemble propagates under the non-Hermitian Hamiltonian H_{NH}

we realize one of the following possibilities:

$$\text{with prob. } 1 - \delta p, \quad |\psi(t + dt)\rangle = \frac{|\psi_0(t + dt)\rangle}{\sqrt{1 - \delta p}}, \quad (2.15)$$

$$\text{with prob. } \delta p_k, \quad |\psi(t + dt)\rangle = \frac{L_k |\psi(t)\rangle}{\sqrt{\delta p_k / dt}}. \quad (2.16)$$

An ensemble of wave functions subject to these dynamics will, on average, reproduce the time dependent solution of the master equation (2.12).

The validity of the calculation relies on time steps much smaller than the time-scale of the coherent and incoherent physical processes. However, the direct implementation discussed above may be reformulated [50, 51] such that quantum jumps are not decided in terms of expression (2.14), linear in the “small” time step dt . Instead, the “no-jump” wave-function $|\psi_0(t)\rangle$ is allowed to evolve until its norm reaches a predetermined random number uniformly distributed between 0 and 1. At this time a jump is made in the manner of Eq. (2.16). In this way integration of

Eq. (2.13) may be left to an accurate and efficient numerical solver. The simulation strategy is illustrated in Fig. 2.3.1. In our implementation to physical examples in this thesis, we use a variant of the Adams-Bashforth method [52] which utilizes adaptive step-size control.

2.3.1 EQUIVALENCE WITH THE MASTER EQUATION

The last section claimed that an ensemble of Monte Carlo wave functions will, on average, reproduce the master equation solution at all times t . We demonstrate this by introducing the statistical operator $\sigma(t) = |\psi(t)\rangle\langle\psi(t)|$. The average value of $\sigma(t + dt)$ may be determined by combining the probabilities found in Eqs. (2.15) and (2.16), that is

$$\begin{aligned}
\bar{\sigma}(t + dt) &= (1 - \delta p) \frac{|\psi_0(t + dt)\rangle\langle\psi_0(t + dt)|}{1 - \delta p} + \sum_k \delta p_k \frac{L_k |\psi(t)\rangle\langle\psi(t)| L_k^\dagger}{\delta p_k / dt} \\
&= |\psi_0(t + dt)\rangle\langle\psi_0(t + dt)| + \sum_k dt L_k |\psi(t)\rangle\langle\psi(t)| L_k^\dagger \\
&= (1 - iHdt - \frac{1}{2}dt \sum_k L_k^\dagger L_k) |\psi(t)\rangle\langle\psi(t)| (1 + iHdt - \frac{1}{2}dt \sum_k L_k^\dagger L_k) \\
&\quad + \sum_k dt L_k |\psi(t)\rangle\langle\psi(t)| L_k^\dagger.
\end{aligned} \tag{2.17}$$

By ignoring factors of dt^2 we find

$$\bar{\sigma}(t + dt) = \sigma(t) - idt[H, \sigma(t)] - \frac{1}{2}dt \sum_k (L_k^\dagger L_k \sigma(t) + \sigma(t) L_k^\dagger L_k) + \sum_k L_k \sigma(t) L_k^\dagger. \tag{2.18}$$

Averaging over different values of $\sigma(t)$ to obtain $\bar{\sigma}(t)$ we make the approximation

$$\frac{\bar{\sigma}(t + dt) - \bar{\sigma}(t)}{dt} \approx \dot{\bar{\sigma}}, \tag{2.19}$$

valid for small dt . The resulting equation takes the form (2.12) from which we conclude that $\bar{\sigma}(t)$ is equal to the master equation solution for the density operator $\rho(t)$ at all times t .

2.4 EFFECTIVE OPERATOR FORMALISM

In this section we review the work of Sørensen and coauthors [53]. There are often very different time-scales involved in an open quantum system. We think, for example, of fast decay from higher lying states into the relatively slow dynamics of ground states in a weakly driven atom. It has been shown [54] that an effective solution is to adiabatically eliminate the unwanted states from the system. This is typically achieved by first separating states of one time-scale with that of the other. After elimination, only the states we are interested in remain. This not a new concept, but often involves lengthy and tedious calculations. Here, we present a set of simple expressions for the effective dynamics in open quantum systems.

We consider an open quantum system consisting of two distinct subspaces, one for the rapidly decaying (excited) states and one for the stable (ground) states (Fig. 2.4.1). The coupling between these two subspace is assumed to be perturbative. Evolution of the density operator ρ is governed by the master equation and decay from the excited states to ground states is described by the Lindblad “jump” operators L_k . In a manner analogous to the Feshbach projection-operator method [55, 56] the open system’s Hamiltonian is divided into four parts

$$H = H_e + H_g + V_+ + V_- , \quad (2.20)$$

where H_e (H_g) is the Hamiltonian for the excited (ground) state manifold and the (de-)excitation operators V_+ (V_-) couple the two subspaces. Dissipation from the excited states is described by the non-Hermitian Hamiltonian

$$H_{\text{NH}} = H_e - \frac{i}{2} \sum_k L_k^\dagger L_k . \quad (2.21)$$

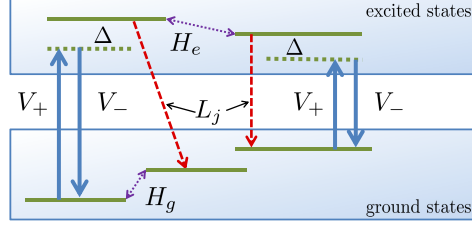


Figure 2.4.1: Subspaces in Hilbert space: The thick (blue) arrows represent the (de-) excitation processes V_+ (V_-) which couple the decaying excited states to the comparatively stable ground states. The Lindblad operators L_j describe jumps from the excited state manifold, depicted by the thick dashed (red) arrows. The dotted (purple) lines illustrate the ground (excited) state couplings described by the Hamiltonian H_g (H_e).

Each of the Lindblad operators L_k correspond to different decay mechanisms, but are strictly defined to begin in the excited state manifold and end up in the ground state manifold. Incorporating the definitions introduced so far, the master equation that describes evolution of the density operator may be written as

$$\dot{\rho} = -i[(H_{\text{NH}} + H_g + V)\rho - \rho(H_{\text{NH}}^\dagger + H_g + V)] + \sum_k L_k \rho L_k^\dagger, \quad (2.22)$$

where $V = V_+ + V_-$. The last term in Eq. (2.22) represents “feeding” of the ground states due to decay from the excited states.

We assume that the coupling between the ground and excited state manifold, described by V_\pm , to be weak compared to the evolution of either manifold. As such it is described as perturbations to the (unperturbed) Hamiltonian $H_0 = H_g + H_{\text{NH}}$. In principle, the resulting second order master equation from a perturbative expansion on the density operator is enough to describe the evolution of the open quantum system. However, if the excited states are essentially unpopulated, we may adiabatically eliminate them thereby restricting dynamics to the ground states. If we assume that interactions within the ground state manifold is weak compared

to the dynamics governed by the non-Hermitian Hamiltonian, we find

$$H_{\text{eff}} = -\frac{1}{2}V_-[H_{\text{NH}}^{-1} - (H_{\text{NH}}^{-1})^\dagger]V_+ + H_g, \quad (2.23)$$

$$L_k^{(\text{eff})} = L_k H_{\text{NH}}^{-1} V_+, \quad (2.24)$$

which is the effective Hamiltonian and Lindblad operators associated with the ground state manifold.

If we make no assumptions about interactions in the ground state manifold we arrive at an alternate expression for the effective operators. Decomposing the excitation operator

$$V_+ = \sum_m V_+^m, \quad (2.25)$$

into a sum of the excitation operators V_+^m corresponding to the m ground states and making the appropriate adjustments, Eqs. (2.23) and (2.24) become

$$H_{\text{eff}} = -\frac{1}{2} \left[V_- \sum_m \left(H_{\text{NH}}^{(m)} \right)^{-1} V_+^m + \text{H.c.} \right] + H_g, \quad (2.26)$$

$$L_k^{\text{eff}} = L_k \sum_m \left(H_{\text{NH}}^{(m)} \right)^{-1} V_+^m, \quad (2.27)$$

where

$$H_{\text{NH}}^{(m)} \equiv H_{\text{NH}} - E_m, \quad (2.28)$$

is the former non-Hermitian Hamiltonian corrected by the energy E_m associated with the m^{th} ground state.

2.5 PROCESS CHARACTERISATION

Characterization of quantum dynamical systems is a prerequisite for high-fidelity quantum computing and information protocols. Two tools created for this purpose are quantum state and quantum process tomography. Quantum state tomography takes the measurement data of a quantum system's unknown state and

identifies the representative density operator ρ . Quantum process tomography is concerned with experimentally characterising a process \mathcal{E} so that the output state may be predicted from any given input state $\rho \rightarrow \mathcal{E}(\rho)$.

Preserving the trace and positivity, a solution for the density matrix $\mathcal{E}(\rho)$ may be described in the operator-sum representation [57]

$$\mathcal{E}(\rho) = \sum_i K_i \rho K_i^\dagger, \quad (2.29)$$

where the Kraus operators K_i act on the system's Hilbert space and obey $\sum_i K_i^\dagger K_i = \mathbb{1}$. Choosing the Hermitian operators $\{E_m\}$ as a basis for the set of all operators on the principal system's Hilbert space¹ we may write any quantum process as

$$\mathcal{E}(\rho) = \sum_{mn} \chi_{mn} E_m \rho E_n^\dagger. \quad (2.30)$$

The characterisation matrix χ_{mn} in Eq. (2.30) is related to the Kraus form (2.29) via the expansion of each $K_i = \sum_m e_{im} E_m$, and the identification $\chi_{mn} = \sum_i e_{im} e_{in}^*$.

Suppose a process is simulated with the master equation, for which the accumulated effect of the unitary and dissipative dynamics on the quantum system is not known *a priori*. From the simulation data, we aim for an efficient method to obtain the full information about \mathcal{E} . In the next section, standard methods of acquiring χ_{mn} , and thus \mathcal{E} , will be shown.

2.5.1 PROCESS CHARACTERISATION SCHEMES

In the following discussion we consider a general quantum system with Hilbert space dimension D . Assuming the map \mathcal{E} is trace-preserving, characterisation of \mathcal{E} is equivalent to a determination of the $D^4 - D^2$ independent elements of χ [36].

Let $\mathcal{O}_{pq} = |p\rangle\langle q|$ for $p, q \in \{1, \dots, D\}$ be a linearly independent basis for the space of $D \times D$ linear operators. Cataloguing the action of the fixed operator basis

¹In a multi-qubit system, an appropriate operator basis might be given by tensor products of the identity and Pauli operators for each qubit.

$\{E_m\}$ on all input matrices, we create the $D^4 \times D^4$ matrix \mathcal{K} :

$$E_m \mathcal{O}_{rs} E_n^\dagger = \sum_{pq} \mathcal{K}_{rs,pq}^{mn} \mathcal{O}_{pq}. \quad (2.31)$$

STANDARD QUANTUM PROCESS CHARACTERISATION

In standard quantum process characterisation (SQPC), the effect of the process \mathcal{E} is determined. Experimentally, D^2 different input states (density matrices) are subjected to the physical process and the resulting output states are measured by quantum state tomography. In a theoretical analysis, the master equation is used to simulate the process and the outcome solution $\mathcal{E}(\mathcal{O}_{rs})$ for input matrices \mathcal{O}_{pq} is expressed as a linear combination in the same operator basis,

$$\mathcal{E}(\mathcal{O}_{rs}) = \sum_{pq} \Lambda_{rs,pq} \mathcal{O}_{pq}. \quad (2.32)$$

Combining Eqs. (2.30), (2.31) and (2.32), we obtain $\sum_{mn} \mathcal{K}_{rs,pq}^{mn} \chi_{mn} = \Lambda_{rs,pq}$ which in matrix form can be written,

$$\mathcal{K} \chi = \Lambda. \quad (2.33)$$

Finding $\{\chi_{mn}\}$ from the simulated $\{\Lambda_{rs,pq}\}$ is now a linear algebra problem, although, in general it is not uniquely determined by Eq. (2.33).

Let us here make an estimate of how the computational resources needed to perform SQPC scale with Hilbert space dimension. Simulating a process with the master equation requires solving D^2 coupled differential equations for each of the D^2 input states; that is, we must solve D^4 differential equations. The solution of Eq. (2.33) requires a decomposition of \mathcal{K} ; using the Cholesky method for example, followed by forward and back substitution for χ . The computational complexity of a straightforward decomposition is $O(D^{12})$ while the substitution operations are each $O(D^8)$. For applications to quantum computing on a register composed of N L -level quantum systems, the product Hilbert space has the dimension $D =$

L^N . We note that if the operators E_m are taken to be $SU(L)$ operator products, the product nature simplifies decomposition of \mathcal{K} into separate $O(L^{12})$ problems.

ANCILLA ASSISTED PROCESS CHARACTERISATION

In ancilla assisted process characterisation (AAPC), instead of composing Λ by propagating separate initial matrices \mathcal{O}_{rs} , all input states are simultaneously represented in a “super” operator

$$\mathcal{O} = \sum_{rs} \mathcal{O}_{rs} \otimes \mathcal{O}_{rs}. \quad (2.34)$$

on the combined principal (P) and ancilla (A) system. This expanded system is now subject to the quantum process, $\mathcal{E}_{P \otimes A}(\mathcal{O}) \rightarrow \mathcal{O}_{\text{out}}$, which acts with the original process \mathcal{E} on the principal system’s component only,

$$\mathcal{O}_{\text{out}} \equiv (\mathcal{E} \otimes \mathbb{1})(\mathcal{O}). \quad (2.35)$$

The identity operator $\mathbb{1}$ in Eq. (2.35) acts on the ancilla’s operator space. From Eq. (2.34) we have $(\mathcal{E} \otimes \mathbb{1})(\mathcal{O}) = \sum_{rs} \mathcal{E}(\mathcal{O}_{rs}) \otimes \mathcal{O}_{rs}$, implying that a single master equation simulation on the expanded system allows us to calculate all $\mathcal{E}(\mathcal{O}_{rs})$. The ancilla system is used to extract separate results,

$$\mathcal{E}(\mathcal{O}_{rs}) = \text{Tr}_A \{ (\mathbb{1} \otimes |s\rangle\langle r|) \mathcal{E}_{P \otimes A}(\mathcal{O}) \}, \quad (2.36)$$

where Tr_A denotes partial trace on the ancilla’s Hilbert space. Then, in a way equivalent to Eq. (2.32) we may expand $\mathcal{E}(\mathcal{O}_{rs})$ into the basis of $\{\mathcal{O}_{pq}\}$ and retrieve the characterisation matrix χ from Eq. (2.33).

Simulating a quantum process with AAPC involves solving D^4 differential equations for the expanded input state. The complexity of solving Eq. (2.33) remains $O(D^{12})$ for decomposition of \mathcal{K} and $O(D^8)$ for forward/backward substitution.

2.6 CONCLUSION

In this chapter we have discussed the concepts important for this thesis. In particular, we have presented assumptions held in upcoming chapters and gathered a set of tools to aid in simulations. Additionally, the formalism for theoretical process characterisation was introduced and two methods reviewed which will serve as comparison to work later in the thesis.

3

Rydberg atoms

Several implementations have proven to be candidates for quantum computation. A good example is ion traps, which utilize the Coulomb force to yield high fidelity gates [58–60]. The caveat with a strong interaction between ions is the strong coupling to stray fields, requiring a carefully controlled experiment. Neutral atoms have gained considerable interest recently as another candidate for quantum information processing [61]. They fulfil most of the DiVincenzo criteria for quantum computation including initialization, successful implementation of quantum gates and readout of results. Neutral atoms also promise scalability as they may be placed in close proximity to each other. The obvious but distinguishing feature of these atoms is that they are electrically neutral. As a result, high-fidelity operations are possible because the atoms do not couple to the environment. Unfortunately, following this reasoning, neutral atoms do not couple with themselves either. Several solutions to the neutral atom’s coupling deficit have been proposed, these in-

clude ground state collisions [21], light mediated dipole-dipole coupling [62] and dipole-dipole coupling of Rydberg states [63].

In this chapter we consider the basics of neutral atoms and the properties that make them attractive for quantum computation. Section 3.1 gives an introduction of the trapping and manipulation of single atoms. Section 3.2 follows on with a discussion of Rydberg atoms and how they might be used to couple neutral atoms. In section 3.3 we develop the single-atom Hamiltonian. Section 3.4 finds an effective form for this Hamiltonian that will be used in later chapters. In section 3.5 we describe a two-atom Hamiltonian that efficiently models Rydberg interactions.

3.1 MANIPULATING SINGLE ATOMS

Cooling, trapping and detecting individual atoms is a necessary first step to experimentally realize quantum logic. This corresponds to two of the DiVincenzo criteria for quantum computation, namely initialization and readout. The study of single neutral atoms, first observed in a magneto-optical trap [64], has progressed rapidly in the context of far-off-resonance traps (FORTs) [65]. Scalability, by loading a large number of individually addressable sites, is also being actively explored [66–72].

Although FORTs accommodate long atomic confinement times, trap lifetime is limited due to collisions with untrapped background atoms. This and, to a less extent, scattering of FORT light reduces the coherence time of an encoded quantum superposition state [73]. Dephasing caused by trapping and field fluctuations may be minimized by an appropriate choice of qubit basis states. A convenient choice is the $f = I \pm 1/2$, $m_f = 0$ hyperfine clock states of alkali atoms with a $S_{1/2}$ ground state and nuclear spin I . These states have a quadratic relative Zeeman shift at zero applied field. All things considered, trapping and coherence times of neutral atoms should reach second time scales [74].

Assuming that an arrangement of single atoms has been trapped, several methods that drive rotations between qubit states have been proposed. One solution is a microwave field resonant to the frequency between qubit states ω_{10} . However, a

specific atom is not addressable under this regime. An alternative approach, which successfully addresses a single atom, combines a microwave field with an electric or magnetic field [75]. A drawback is the difficulty of shielding neighbouring sites from off-resonance perturbations. Finally, two-photon Raman transitions, facilitated by focused lasers, offer fast ground state manipulation with minimal crosstalk to sites nearby ($\sim 10 \mu\text{m}$) [76]. It has the further benefit of allowing atoms that are separated by large distances, as compared to the laser’s beam waist, to be addressed simultaneously.

3.2 RYDBERG ATOMS AND THEIR INTERACTIONS

Atoms excited into states with principal quantum number $n \gg 1$, the Rydberg states, display exaggerated and remarkable properties. As more technology has become available, Rydberg atoms have found applications in a growing number of studies [77, 78]. In particular, the strong dipole-dipole interaction between Rydberg atoms in close proximity allows novel approaches to numerous quantum protocols. Examples are single-atom state preparation [68], fast quantum state detection [79], and collective encoding of multi-qubit registers [80]. Here, we will discuss properties of Rydberg atoms and see how the “Rydberg blockade” may be used to create gates for quantum computation.

3.2.1 BINARY INTERACTIONS

Rydberg atoms may exhibit long range dipole-dipole and van der Waals interactions provided there is a degeneracy in the energy-level spectrum for a pair of atoms. This is satisfied given the two-atom, or pair, states are dipole-dipole coupled, meaning they preserve total angular momentum. The dipole-dipole interaction may be understood by considering two classical dipoles with dipole moments $\boldsymbol{\mu}_1$ and $\boldsymbol{\mu}_2$. Their interaction energy in atomic units is

$$V_{dd}(\mathbf{R}) = \frac{\boldsymbol{\mu}_1 \cdot \boldsymbol{\mu}_2}{|\mathbf{R}|^3} - 3 \frac{(\boldsymbol{\mu}_1 \cdot \mathbf{R})(\boldsymbol{\mu}_2 \cdot \mathbf{R})}{|\mathbf{R}|^5}, \quad (3.1)$$

where \mathbf{R} is the distance vector connecting the dipoles. The second term in Eq. (3.1) accounts for the angular dependence of the interaction energy and will be neglected in this discussion for simplicity.

In the corresponding quantum mechanical description, a dipole is represented with the dipole operator $e\mathbf{r}$, with matrix elements $\mu_{ij} = \langle i|e\mathbf{r}|j\rangle$, where e is electron charge and \mathbf{r} is the position operator. For atom 1 (2) initially in state $|i_1\rangle$ ($|i_2\rangle$) the interaction energy becomes

$$V_{dd}(\mathbf{R}) \propto \frac{1}{R^3} \sum_{|i'_1\rangle, |i'_2\rangle} \langle i_1|e\mathbf{r}_1|i'_1\rangle \langle i_2|e\mathbf{r}_2|i'_2\rangle \quad (3.2)$$

$$= \frac{1}{R^3} \sum_{|i'_1, i'_2\rangle} \langle i_1 i_2 | e^2 \mathbf{r}_1 \mathbf{r}_2 | i'_1 i'_2 \rangle. \quad (3.3)$$

For the purposes of this discussion we only need to consider transitions from the initial Rydberg state $|r\rangle$ to the adjacent angular momentum states, $|a\rangle$ and $|b\rangle$, all others add no significant contribution [74]. In Eq. (3.3) we moved from the single-atom basis into the pair basis in order to elucidate the energy shifts induced by the dipole-dipole interaction (see Fig. 3.2.1). The initial state $|rr\rangle$ is coupled by $V_{dd}(\mathbf{R}) = (\mu_{ra}^{(1)} \mu_{rb}^{(2)})/R^3$ to $|ab\rangle$, offset by the energy defect

$$\delta = E_{|ab\rangle} - E_{|rr\rangle} = E_{|a\rangle} + E_{|b\rangle} - 2E_{|r\rangle}, \quad (3.4)$$

where the pair state energy $E_{|i_1 i_2\rangle}$ is the sum of the single-atom energies $E_{|i_1\rangle}$ and $E_{|i_2\rangle}$. Assuming to be in the pair state basis $\{|rr\rangle, |ab\rangle\}$ we diagonalize the Hamiltonian

$$H = \begin{pmatrix} 0 & V_{dd}(\mathbf{R}) \\ V_{dd}(\mathbf{R}) & \delta \end{pmatrix}, \quad (3.5)$$

which describes the system of closely degenerate states, and find the eigen-energies

$$U_{\pm} = \frac{1}{2}(\delta \pm \sqrt{\delta^2 + 4V_{dd}^2(\mathbf{R})}). \quad (3.6)$$

From Eq. (3.6) we consider two regimes. In the limit of near degeneracy $\delta \ll$

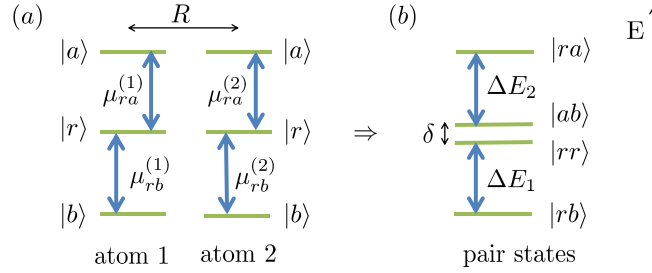


Figure 3.2.1: Rydberg-Rydberg interactions: (a) Two three-level atoms separated by a distance R . The dipole matrix elements μ_{ij} couple the Rydberg states. (b) Two pair states, $|rr\rangle$ and $|ab\rangle$, are nearly degenerate with a small energy defect δ . Rydberg atoms with this pair state level structure experience strong long-range interactions.

$V_{dd}(R)$, the eigen-energies are $U_{\pm} = \pm V_{dd}(R)$ which scales as $1/R^3$. In this regime interactions are of dipole-dipole form. Conversely, in the limit of large energy defects $\delta \gg V_{dd}(R)$, the eigen-energies are $U_{+} = \delta + V_{dd}^2(R)/\delta$ and $U_{-} = -V_{dd}^2(R)/\delta$, both scaling like $1/R^6$ of van der Waals form.

To obtain some physical insight, Fig. 3.2.2 depicts the dependence of interaction strength $U(R)$ of singly charged ions, ground-state Rb atoms, and Rydberg atoms as a function of the inter-atom separation R . Even at close inter-atomic distances of $\sim 1 \mu\text{m}$ interactions between ground-state neutral atoms are weak, suggesting that they may be initialized in a tight and stable configuration. In contrast, Rubidium atoms excited into the 100s Rydberg state display very strong interactions. At small distances we see the expected $1/R^3$ scaling, approaching Förster resonance as $R \rightarrow 0$. Beyond $\sim 10 \mu\text{m}$, interactions become of van der Waals form. An added feature of Rydberg interactions is that, as opposed to the uncontrollable ion-ion Coulomb force which is always “on”, it may be turned “off” by de-exciting one of the atoms to the ground state.

The van der Waals interaction typically scales with n^{11} [81] and the resonant Förster interactions with n^4 , so it is generally advantageous to work with the highest quantum number possible. We see this highlighted in Fig. 3.2.2 where for $n = 100$ the ratio of Rydberg interaction to ground-state interaction is approximately

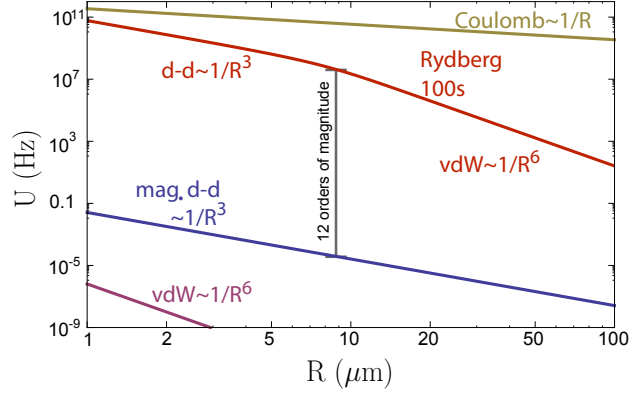


Figure 3.2.2: Two-atom interaction strength of ionic (top line), ground-state Rubidium (bottom two lines) and Rydberg excited Rubidium (second line from top) atoms as a function of the inter-particle distance. The Rydberg atoms are excited to the 100s state. Reproduced from [74]

10^{12} [74]. However, there is an upper limit to n based on practical considerations. This includes addressability of decreasing discrete energy level separations, ionization, and collisions with valence electrons of neighbouring atoms [82].

3.2.2 QUANTUM COMPUTATION WITH RYDBERG ATOMS

A feature of Rydberg interactions that has great promise for quantum information processing is the *Rydberg blockade*. This effect, demonstrated by several groups [83–85], arises due to the energy shift \mathcal{B} that blocks two or more atoms from occupying the Rydberg state while they are driven by an excitation laser (Fig. 3.2.3). Here, we discuss quantum computing implementations involving the coherent excitation of a single atom into the Rydberg state [63, 86] - although other possibilities exist [87, 88]. The success of this approach relies on the atoms being close enough for strong interactions while still allowing individual control. The loading and addressing requirements have been achieved by several groups [89, 90] with the former reporting Rydberg Rabi frequencies of $\Omega/2\pi = 1.15$ MHz which translates into π pulse times of approximately 440 ns [91].

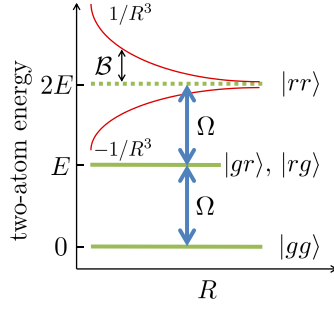


Figure 3.2.3: Rydberg blockade: Two atoms are separated by distance R and both have the ground state $|g\rangle$ coupled to the Rydberg state $|r\rangle$ with Rabi frequency Ω . In the two-atom state $|rr\rangle$ the atoms strongly interact, causing a “blockade” energy shift of $\mathcal{B} \sim \pm 1/R^3$. When $\mathcal{B} > \Omega$, the laser coupling the singly excited states to the doubly excited state is off-resonant, allowing only one atom to excite into the Rydberg state.

The Rydberg interaction is ideally suited for neutral atom quantum gates [63, 87], the building blocks of quantum computation. By way of example we consider the controlled-Z (C_Z) gate with the unitary matrix

$$U_{C_Z} = \begin{pmatrix} 1 & 0 & 0 & 0 \\ 0 & -1 & 0 & 0 \\ 0 & 0 & -1 & 0 \\ 0 & 0 & 0 & -1 \end{pmatrix}, \quad (3.7)$$

written in the computational basis $\{|00\rangle, |01\rangle, |10\rangle, |11\rangle\}$. The C_Z gate is a two-qubit gate consisting of a control (c) and target (t) qubit, where control is achieved using Rydberg-Rydberg interactions. The qubit states are $|0\rangle$ and $|1\rangle$, where $|1\rangle$ is coupled to the Rydberg state $|r\rangle$ via an excitation laser with an arbitrary Rabi frequency (ideal gate). An ideal C_Z gate may be implemented in a sequence of three pulses [63], depicted in Fig. 3.2.4: (pulse 1), the control atom’s population is transferred from $|1\rangle$ to $|r\rangle$ via a π -pulse. A 2π -pulse (pulse 2) on the target atom induces the population transfer $|1\rangle \rightarrow |r\rangle \rightarrow |1\rangle$. Finally (pulse 3), the control atom’s population in $|r\rangle$ is returned to $|1\rangle$. If the control atom has population in $|r\rangle$, excitation of the target atom’s population will be off-resonant. Assuming perfect

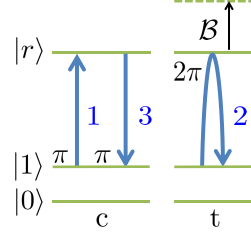


Figure 3.2.4: Controlled-Z gate: (pulse 1) a resonant transfer between the qubit state $|1\rangle$ and Rydberg state $|r\rangle$ of the control atom c . (pulse 2) subsequent coherent excitation and de-excitation between $|1\rangle$ and $|r\rangle$ of the target atom t . This performs a Pauli-Z operation on $|1\rangle$, unless the control atom is excited and blocks it with an energy shift \mathcal{B} . (pulse 3) de-excitation of the control atom.

blockade, atoms in the initial state configurations, $|01\rangle$, $|10\rangle$ and $|11\rangle$ will have precisely one atom coupled to $|r\rangle$, thereby picking up an overall π phase shift on completion of the pulse sequence. Otherwise, the two-atom state that begins in $|00\rangle$ will have neither atom coupled to the Rydberg state and no phase is acquired. In this way we reproduce the unitary (3.7).

In addition to the errors that plague single-atom operations, there are other experimental restrictions to consider. The main contributors harming two-atom operations are atomic motion, preventing perfect transfer to the Rydberg level and motional heating of atoms during transfer to the Rydberg state [73]. These sources of decoherence are highly dependent on the input state, seen in reference to Fig. 3.2.4: The state $|00\rangle$ is not coupled to the Rydberg state during the entire operation, avoiding Rydberg related errors. In all other cases, at least one atom atom performs the $|1\rangle$ to $|r\rangle$ transition (with varying success), thereby reducing gate fidelity.

In the regime of blockade energies much larger than the driving Rabi frequency ($\mathcal{B} \gg \Omega$), leading-order contributions to intrinsic error of a gate operation are finite Rydberg state lifetime and imperfect blockade. Averaging over the four pos-

sible input states, the gate error is [73, 74]

$$E = \frac{7\pi}{4\Omega\tau} \left(1 + \frac{\Omega^2}{\omega_{10}^2} + \frac{\Omega^2}{7\mathcal{B}^2} \right) + \frac{\Omega^2}{8\mathcal{B}^2} \left(1 + 6\frac{\mathcal{B}^2}{\omega_{10}^2} \right). \quad (3.8)$$

The first term, scaling like $1/\tau$, is associated with spontaneous emission, while the second accounts for error caused by an imperfect blockade. In the limit $\omega_{10} \gg (\mathcal{B}, \Omega)$, we are able to derive a simple expression for the Rabi frequency that minimizes the error,

$$\Omega_{\text{opt}} = (7\pi)^{1/3} \frac{\mathcal{B}^{2/3}}{\tau^{1/3}}. \quad (3.9)$$

Substituting Ω in Eq. (3.8) for Ω_{opt} , we arrive at a minimum for the averaged gate error,

$$E_{\text{min}} = \frac{3(7\pi)^{2/3}}{8} \frac{1}{(\mathcal{B}\tau)^{2/3}}. \quad (3.10)$$

To illustrate Eq. (3.10) for the ^{87}Rb ns states, Fig. 3.2.5 depicts the error for a range of atomic numbers $50 \leq n \leq 200$ as a function of the inter-atomic separation R . If excitation to the $n = 200$ state can be achieved, we are able to perform high-fidelity C_Z operations at distances up to $R = 50 \mu\text{m}$.

3.3 SINGLE-ATOM HAMILTONIAN

In this section we develop a single-atom Hamiltonian for a four-level system with driving lasers. The material presented is not original but is useful as a point of reference. It provides the groundwork for the next section and the subtleties found there are introduced here.

In the presence of an external field, the Hamiltonian describing an electron bound to an atom is [92]

$$H = H_0 + H_{\text{int}} \quad (3.11)$$

where

$$H_0 = \frac{\mathbf{P}^2}{2m} + V(R) \quad \text{and} \quad H_{\text{int}} = e\mathbf{r} \cdot \mathbf{E}(t). \quad (3.12)$$

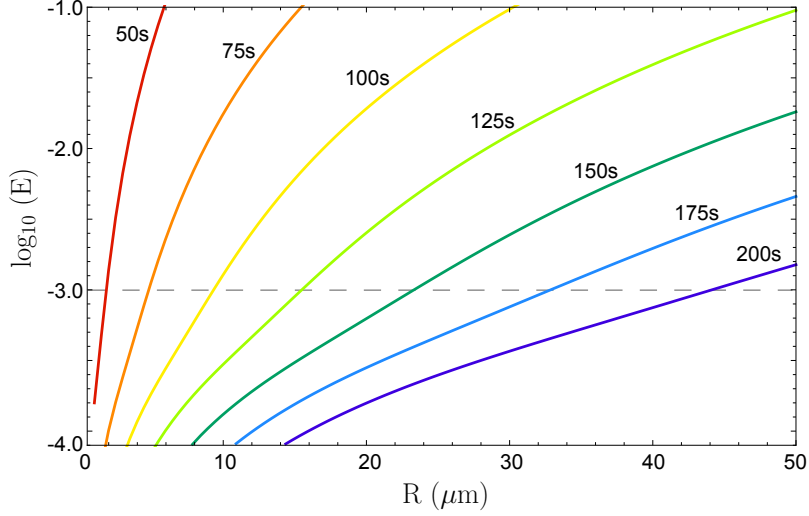


Figure 3.2.5: Intrinsic error E involved in a C_Z gate as a function of the separation between the control and target atom. Lifetimes, in the order of increasing n , are $\tau = 70, 180, 340, 570, 860, 1200$ and $1600 \mu\text{s}$. The dashed line represents the cutoff for a useful C_Z operation. Reproduced from [74]

In the Hamiltonian H_0 describing the external-field-free part, $V(R)$ is the usual Coulomb interaction binding the electron to the nucleus, R is the inter-particle distance, m is the electron mass and $\mathbf{P} = -i\nabla$. In the Hamiltonian H_{int} describing the external field, $\mathbf{E}(t)$ is the time-dependent electric field and, given e is the electron charge, $\mathbf{d} = -e\mathbf{r}$ is the dipole moment. The Hamiltonian assumes the dipole approximation, taking the wave-length of the laser used to drive transitions between atomic energy levels to be much larger than typical atomic dimensions.

The system under consideration has four levels. These include the qubit states $|0\rangle$ and $|1\rangle$, the intermediate state $|p\rangle$ and the Rydberg state $|r\rangle$. For convenience we rewrite H into the basis of the eigen-vectors of H_0 . The external-field-free part falls into diagonal form

$$H_0 = \sum_{k \in \{0,1,p,r\}} E_k |k\rangle \langle k|, \quad (3.13)$$

where E_k is the energy of state $|k\rangle$. To express H_{int} in this basis we assume that $|p\rangle$ has opposite parity to all other relevant eigen-states. By Laporte's selection rule, all elements of the dipole operator sharing the same parity vanish, that is, $\langle p|\mathbf{d}|p\rangle = \langle i|\mathbf{d}|i'\rangle = 0$, where $i, i' \in \{1, r\}$. Writing down what is left, the interaction Hamiltonian becomes

$$H_{\text{int}} = - (\mathbf{d}_{1,p}|1\rangle\langle p| + \mathbf{d}_{p,r}|p\rangle\langle r| + \text{H.c.}) \cdot \mathbf{E}(t) \quad (3.14)$$

where H.c. denotes the Hermitian conjugate of the two previous terms.

In this discussion, coherent excitation from $|1\rangle$ to $|r\rangle$ is a two photon process using a ‘‘red’’ (‘‘blue’’) beam tuned by an amount Δ to the red (blue) of the intermediate state $|p\rangle$. The electric fields of the red and blue lasers are labelled $\mathbf{E}_R(t)$ and $\mathbf{E}_B(t)$, respectively. Each electric field vector may be decomposed into positive and negative frequency components, that is, $\mathbf{E}_j(t) = \mathbf{E}_j e^{+i\omega_j t} + \mathbf{E}_j e^{-i\omega_j t}$. The interaction Hamiltonian now becomes

$$H_{\text{int}} = - (\mathbf{d}_{1,p}|1\rangle\langle p| + \mathbf{d}_{p,1}|p\rangle\langle 1|) \cdot (\mathbf{E}_R e^{i\omega_R t} + \mathbf{E}_R e^{-i\omega_R t}) \\ - (\mathbf{d}_{p,r}|p\rangle\langle r| + \mathbf{d}_{r,p}|r\rangle\langle p|) \cdot (\mathbf{E}_B e^{i(\omega_B + \delta E_r)t} + \mathbf{E}_B e^{-i(\omega_B + \delta E_r)t}). \quad (3.15)$$

Contributions due to off-resonant coupling of $|0\rangle$ to $|p\rangle$ is heavily suppressed by the qubit state energy splitting $\omega_{10} \sim 7$ GHz and can be ignored. The small addition to the blue lasers frequency δE_r will compensate for any time-dependence the blue Rabi frequency acquire when moving into a rotating frame.

For U an arbitrary unitary operator, $H' = i\dot{U}U^\dagger + UH U^\dagger$ is the Hamiltonian H in a rotating frame. This translates to

$$H' = H'_1 + H'_2, \quad (3.16)$$

where

$$H'_1 = i\dot{U}U^\dagger + UH_0U^\dagger \quad \text{and} \quad H'_2 = UH_{\text{int}}U^\dagger. \quad (3.17)$$

Because we are primarily interested in the transition frequencies, it is natural to

move into the frame of the detuning from $|p\rangle$. Thus, we choose

$$U = \exp\left(-it\left[\sum_{k \in \{0,1,p,r\}} (\delta_k - E_k)|k\rangle\langle k|\right]\right), \quad (3.18)$$

where $\delta_k \in \{\Delta + \delta E_0, \Delta, 0, \Delta - \delta E_r\}$. In the next section we explain why the small frequencies δE_0 and δE_r are added and what values they should take.

Since the exponent of U commutes with its partial derivative with respect to time, then $\dot{U} = -iU(\sum_k (E_k + \delta_k)|k\rangle\langle k|)$, and H'_1 in Eq. (3.17) becomes

$$\begin{aligned} H'_1 &= U \left(\sum_k (\delta_k - E_k)|k\rangle\langle k| \right) U^\dagger + U \left(\sum_k E_k |k\rangle\langle k| \right) U^\dagger \\ &= \sum_k \delta_k |k\rangle\langle k|, \end{aligned} \quad (3.19)$$

using the commutation relations $[U, |k\rangle\langle k|] = 0 \forall k$. With a little work, it is also found that

$$\begin{aligned} H'_2 &= - \left(\mathbf{d}_{1,p} \cdot \mathbf{E}_R |1\rangle\langle p| + \mathbf{d}_{p,r} \cdot \mathbf{E}_B |p\rangle\langle r| \right) + \text{H.c.} \\ &\quad - \left(\mathbf{d}_{1,p} \cdot \mathbf{E}_R e^{-2i\omega_R t} |1\rangle\langle p| + \mathbf{d}_{p,r} \cdot \mathbf{E}_B e^{-2i(\omega_B + \delta E_r)t} |p\rangle\langle r| \right) + \text{H.c.}, \end{aligned} \quad (3.20)$$

where we have used

$$U|m\rangle\langle n| = \exp\left(-it(\delta_m - E_m)\right)|m\rangle\langle n|, \quad (3.21)$$

and the corresponding equality for $|m\rangle\langle n|U^\dagger$. In calculating Eq. (3.20) it is helpful to use what we know about the difference between resonance and light frequencies

$$\Delta = (E_1 - E_p) + \omega_R = (E_r - E_p) - \omega_B, \quad (3.22)$$

depicted in Fig. 3.3.1. It may be plainly seen in Eq. (3.20) that the terms in the first set of parentheses dominate those in the second set. Over the duration of an experiment we can assume these terms effectively average to zero, which in the

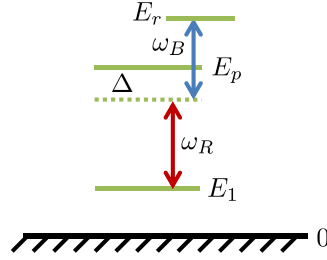


Figure 3.3.1: Energy level structure of a Rydberg atom relevant to the Hamiltonian in the text: E_i refers to the energy of the i^{th} state.

rotating wave approximation means they may be neglected.

Finally, defining the Rabi frequency $\Omega_j = 2\mathbf{d}_{x,y} \cdot \mathbf{E}_j$ (assumed real) we have a simplified expression for the system's Hamiltonian

$$H' = \sum_k \delta_k |k\rangle\langle k| - \frac{\Omega_R}{2} (|1\rangle\langle p| + |p\rangle\langle 1|) - \frac{\Omega_B}{2} (|p\rangle\langle r| + |r\rangle\langle p|). \quad (3.23)$$

For the purposes of clarity we denote H' as H for the remainder of this thesis.

3.4 EFFECTIVE SINGLE-ATOM HAMILTONIAN

In this section we develop an effective Hamiltonian that provides a numerically efficient and stable model for upcoming chapters. The Hamiltonian as it stands has vastly different time-scales ($\Delta \gg \Omega_R, \Omega_B$) and operates in a large Hilbert space. The strategy employed here will be to isolate the dynamics that we are interested in and adiabatically eliminate the rest. We will also find effective operators for the decoherence processes involved.

Reminded that the system is in the rotating frame of the previous section we

may dissect Eq. (3.23) as follows: $H = H_g + H_e + V$, where

$$H_g = (\Delta + \delta E_0)|0\rangle\langle 0| + \Delta|1\rangle\langle 1| + (\Delta - \delta E_r)|r\rangle\langle r| \quad (3.24)$$

$$H_e = 0 \quad (3.25)$$

$$\begin{aligned} V &= V_+^R + V_-^R + V_+^B + V_-^B \\ &= -\frac{\Omega_R}{2}(|1\rangle\langle p| + |p\rangle\langle 1|) - \frac{\Omega_B}{2}(|p\rangle\langle r| + |r\rangle\langle p|), \end{aligned} \quad (3.26)$$

summarized in Fig.3.4.1. The physical significance of δE_0 and δE_r will be explained in section 3.4.1. Decohering processes are governed by

$$L_{\gamma_p,j} = \sqrt{c_j\gamma_p} |j\rangle\langle p|, \quad (3.27)$$

$$L_{\gamma_d} = \sqrt{\gamma_d}(\mathbb{1} - 2|r\rangle\langle r|), \quad (3.28)$$

$$L_{\gamma_r} = \sqrt{\gamma_r} |p\rangle\langle r|. \quad (3.29)$$

In order, these Lindblad operators L describe decay from $|p\rangle$, dephasing of $|r\rangle$ and decay from $|r\rangle$ with rates of γ_p , γ_d and γ_r respectively. In Eq. (3.27) the weights c_j for $j \in \{0, 1, g\}$ are the branching ratios of the intermediate state's decay into state $|j\rangle$. In Eq. (3.28), $\mathbb{1}$ is shorthand for the identity operator. It is appropriate here to discuss $L_{\gamma_p,g}$ because the ‘‘atom loss state’’ $|g\rangle$ does not feature in the system's Hamiltonian. Decay events into $|g\rangle$ do not couple back into the system, making a simple count of (Monte Carlo) jumps into this loss state sufficient to account for its contribution to the error. Because an atom in $|g\rangle$ no longer contributes to system dynamics, the Monte Carlo trajectory may be disposed if a jump of this sort is detected.

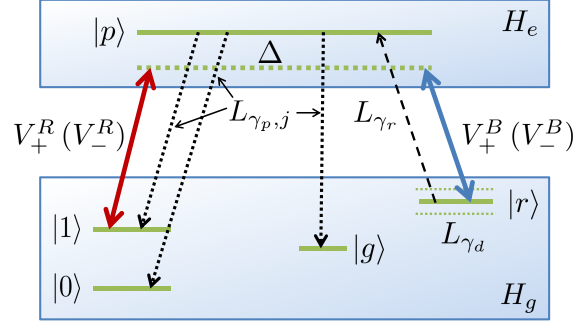


Figure 3.4.1: Towards an effective Rydberg system: The five level system divided into the ground and excited state manifolds. The ground states are coupled to the “excited” intermediate state $|p\rangle$ by the (de-)excitation operators V_+^x (V_-^x), where $x = R$ (B) represents coupling by the red (blue) detuned laser. The operators L_y , where $y = \gamma_p, \gamma_r$ or γ_d , represent various decoherence processes as detailed in the text.

3.4.1 ADIABATIC ELIMINATION

If nonperturbative effects between ground states are included, we remember from section 2.4 that

$$H_{\text{eff}} = -\frac{1}{2} \left[V_- \sum_l \left(H_{\text{NH}}^{(l)} \right)^{-1} V_+^l + \text{H.c.} \right] + H_g, \quad (3.30)$$

where the index l runs over the ground states $|0\rangle, |1\rangle$ and $|r\rangle$. The non-Hermitian Hamiltonian for each ground state is

$$H_{\text{NH}}^{[l]} = - \left(\frac{i\Gamma}{2} |p\rangle\langle p| + \delta_l \mathbb{1} \right), \quad (3.31)$$

where δ_l indexes the energy associated with state $|l\rangle$ (c.f. Eq. (3.18)) and $\Gamma = \sum_j c_j \gamma_p$. The contributions of L_{γ_a} and L_{γ_r} are not included in Eq. (3.31) because they do not meet the formalism’s criterion that a jump takes the atom from the excited state manifold to one of the ground states.

Having all the pieces to solve Eq. (3.30) we find

$$H_{\text{eff}} = \delta E_0 |0\rangle\langle 0| + \left(\frac{\Delta \Omega_R^2}{4\Delta^2 + \gamma^2} \right) |1\rangle\langle 1| + \left(\frac{(\Delta - \delta E_r) \Omega_B^2}{4(\Delta - \delta E_r)^2 + \gamma^2} - \delta E_r \right) |r\rangle\langle r| + \left(\frac{(2\Delta - \delta E_r) \Omega_R \Omega_B}{8\Delta(\Delta - \delta E_r) + 2\gamma^2} |1\rangle\langle r| + \text{H.c.} \right) + \Delta \mathbb{1}. \quad (3.32)$$

Recognizing that $\Delta \mathbb{1}$ only contributes to the overall phase, we may immediately subtract it from the diagonal. Without the addition of δE_r in Eq. (3.32) a difference between the Rabi frequencies Ω_R and Ω_B would cause an energy mismatch between the states $|1\rangle$ and $|r\rangle$. The stark shift induced by this mismatch leads to sub-optimal transitions between these states. By introducing the offset δE_r , which can be approximated by $\sqrt{\Omega_R^2 - \Omega_B^2}$, to the blue laser's frequency, the discrepancy may be corrected. Thus, we are left with

$$H_{\text{eff}} = \left(\delta E_0 - \frac{\Delta \Omega_R^2}{4\Delta^2 + \gamma^2} \right) |0\rangle\langle 0| + \underbrace{\frac{(2\Delta - \delta E_r) \Omega_R \Omega_B}{8\Delta(\Delta - \delta E_r) + 2\gamma^2}}_{\Omega_{\text{eff}}/2} |1\rangle\langle r| + \text{H.c.}, \quad (3.33)$$

where the coefficient of $|1\rangle\langle r|$ is half of the effective Rabi frequency Ω_{eff} . We may now employ δE_0 to remove the contribution that the population in $|0\rangle$ has on the effective Hamiltonian. Without it, there would be a slow rotation of the population in $|0\rangle$, which would be detrimental to the evolution of a qubit state superposition. In the end we are left with a four-level (including loss state) Hamiltonian with an effective Rabi frequency coupling the qubit state $|1\rangle$ with the Rydberg state $|r\rangle$.

To model dynamics in an open quantum system the effective Lindblad operators may be calculated as follows

$$L_k^{(\text{eff})} = L_k \sum_l \left(H_{\text{NH}}^{(l)} \right)^{-1} V_+^l. \quad (3.34)$$

However, use of Eq. (3.34) is restricted to events that start in the excited state manifold and decay into the ground state manifold. The operators (3.27) satisfy this

condition and become

$$L_{\gamma_p, j}^{(\text{eff})} = \frac{\sqrt{c_j \gamma_p} \Omega_R}{2\Delta - i\gamma} |j\rangle\langle 1| + \frac{\sqrt{c_j \gamma_p} \Omega_B}{2(\Delta - \delta E_r) - i\gamma} |j\rangle\langle r|. \quad (3.35)$$

The remaining operators (3.28) and (3.29) are not sensitive to the detuning Δ and, thus, do not have a strictly effective form. This being said, because the intermediate state has been adiabatically removed, they are required to operate in the ground state manifold. Dephasing of the Rydberg state confined to the ground states is described by

$$L_{\gamma_d, r}^{(\text{eff})} = \sqrt{\gamma_d} (\mathbb{1}_G - 2|r\rangle\langle r|), \quad (3.36)$$

where $\mathbb{1}_G$ is the identity operator in the ground-state manifold.

Decay from the Rydberg state poses an interesting problem: Spontaneous emission of $|r\rangle$ implies decay into $|p\rangle$, a state which been adiabatically removed. To solve this we exploit the rapid decay rate of the intermediate state. The effective operator describing Rydberg decay remains the same as for the original system, that is

$$L_{\gamma_r}^{(\text{eff})} = L_{\gamma_r} = \sqrt{\gamma_r} |p\rangle\langle r|, \quad (3.37)$$

but in the case of an event, we temporarily reintroduce the intermediate state. System dynamics is temporarily confined to the provisional state $|p\rangle$, where it then quickly decays, making one of the jumps described by the operators (3.27). In practice, this does not mean returning to a five level description, as the intermediate state may “borrow” the loss state during its short appearance. We refer to Fig. 3.4.2 for a visualization of the effective Hamiltonian and decohering processes.

Thus far, we have presented a model for two photon excitations in an open quantum Rydberg system. Two significant sources of decoherence are considered: First, spontaneous emission from both the high-lying Rydberg state and the state mediating the two-photon exchange. Second, error caused by dephasing of the

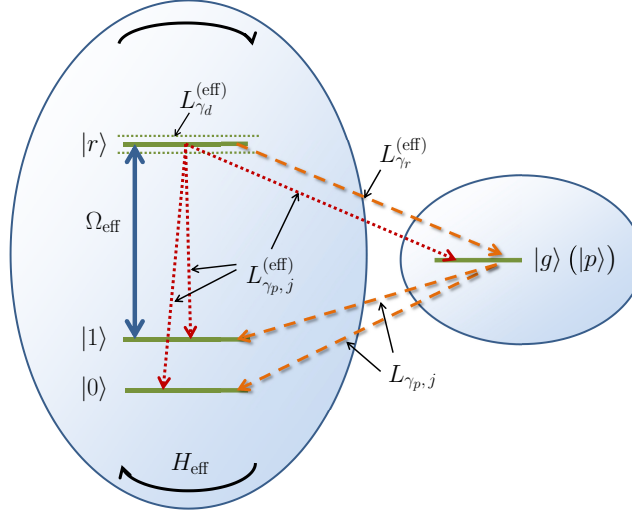


Figure 3.4.2: For numerical efficiency the short-lived, intermediate state $|p\rangle$ is adiabatically eliminated and yields an effective description with couplings (Ω_{eff}) and dissipation terms ($\hat{L}_{\gamma_d}, \hat{L}_{\gamma_{p,j}}$) shown in the left part of the figure. For convenience, $|p\rangle$ is formally reintroduced to also represent decay events from $|r\rangle$ (see text).

Rydberg state. Originally a five level system (including loss state), we were able to reduce the complexity by adiabatically eliminating the mediating $|p\rangle$ state. For the resulting system a set of effective operators was calculated that ensure the time-scales for all processes are of the same order. A careful study of the Rydberg state's decay was needed as it involved feeding of the previously eliminated mediating state.

3.5 TWO-ATOM HAMILTONIAN

If an atom achieves excitation to the Rydberg state, it will block a nearby atom attempting the same transition via the Rydberg-Rydberg interaction. In this thesis, we consider a Rydberg gate in the limit of a Rydberg blockade energy shift (\mathcal{B}) much larger than than the Rabi frequency of the Rydberg state excitation Ω_{eff} . Because typical shifts achieved in experiment are of an order of magnitude larger than the excitation Rabi frequency, there are two very different time-scales introduced

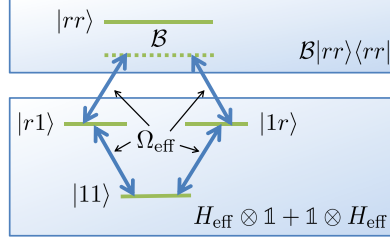


Figure 3.5.1: Adiabatic elimination of the doubly excited Rydberg state: When the Rydberg blockade $\mathcal{B} \gg \Omega_{\text{eff}}$ there is only a weak coupling between the ground states and the doubly excited Rydberg state $|rr\rangle$.

in a numerical simulation. This section presents an efficient numerical implementation of interacting two-atom dynamics.

The two-atom state $|rr\rangle$, with energy \mathcal{B} , is a candidate for “rough adiabatic elimination” [93] as it fulfils two criteria: The state $|rr\rangle$ is only weakly coupled to any other state and in a quantum computational operation, population does not begin in the Rydberg state. In the language of the previous section, the system in which both atoms occupy the Rydberg state lies in the excited state manifold, as depicted in Fig. 3.5.1. Toward an effective Hamiltonian we assume that $|rr\rangle$ undergoes no evolution, or its population c_{rr} remains static, $\dot{c}_{rr}(t) = 0$. Schrödinger’s equation for the evolution of the state $|\psi\rangle = [\dots, c_{r1}, \dots, c_{1r}, \dots, c_{rr}]^T$ under the Hamiltonian $\mathbb{1} \otimes H_{\text{eff}} + H_{\text{eff}} \otimes \mathbb{1} + \mathcal{B}|rr\rangle\langle rr|$ is

$$\left\{ \begin{array}{l} \vdots \\ i\dot{c}_{r1}(t) = \frac{\Omega_{\text{eff}}}{2} c_{rr} \\ \vdots \\ i\dot{c}_{1r}(t) = \frac{\Omega_{\text{eff}}}{2} c_{rr} \\ \vdots \\ i\dot{c}_{rr}(t) = \frac{\Omega_{\text{eff}}}{2} c_{r1} + \frac{\Omega_{\text{eff}}}{2} c_{1r} + \mathcal{B} c_{rr}, \end{array} \right. \quad (3.38)$$

$$\left\{ \begin{array}{l} \vdots \\ i\dot{c}_{r1}(t) = \frac{\Omega_{\text{eff}}}{2} c_{rr} \\ \vdots \\ i\dot{c}_{1r}(t) = \frac{\Omega_{\text{eff}}}{2} c_{rr} \\ \vdots \\ i\dot{c}_{rr}(t) = \frac{\Omega_{\text{eff}}}{2} c_{r1} + \frac{\Omega_{\text{eff}}}{2} c_{1r} + \mathcal{B} c_{rr}, \end{array} \right. \quad (3.39)$$

$$\left\{ \begin{array}{l} \vdots \\ i\dot{c}_{r1}(t) = \frac{\Omega_{\text{eff}}}{2} c_{rr} \\ \vdots \\ i\dot{c}_{1r}(t) = \frac{\Omega_{\text{eff}}}{2} c_{rr} \\ \vdots \\ i\dot{c}_{rr}(t) = \frac{\Omega_{\text{eff}}}{2} c_{r1} + \frac{\Omega_{\text{eff}}}{2} c_{1r} + \mathcal{B} c_{rr}, \end{array} \right. \quad (3.40)$$

where we have left out decoherence effects for simplicity.

Under the conditions above, we see from Eq. (3.40) that c_{rr} may be rewritten as a sum of the other states,

$$c_{rr} = -\frac{\Omega_{\text{eff}}}{2\mathcal{B}} c_{r1} - \frac{\Omega_{\text{eff}}}{2\mathcal{B}} c_{1r}. \quad (3.41)$$

In this description of c_{rr} , the population of $|rr\rangle$ may be considered slaved to the dynamics of the other states. Substituting Eq. (3.41) back into Eqs. (3.40) and (3.40), we find

$$i\dot{c}_{r1}(t) = i\dot{c}_{1r}(t) = -\frac{\Omega_{\text{eff}}^2}{4\mathcal{B}} c_{r1} - \frac{\Omega_{\text{eff}}^2}{4\mathcal{B}} c_{1r}, \quad (3.42)$$

an effective Hamiltonian for a system without the state $|rr\rangle$. Now, the relevant terms in this Hamiltonian go as the inverse of the blockade frequency \mathcal{B} . Whereas before a high-fidelity gate facilitated by increasing \mathcal{B} pushed us further away from numerical feasibility, we are now able to investigate regimes with perfect blockade. Assuming that only two atoms attempt to access the Rydberg state at any one time, this method may be extended in a straightforward way to a multi-atom system with numbers $N > 2$ atoms. This allows us to simulate one atom controlling all others inside the Rydberg radius.

3.6 CONCLUSION

In this chapter we discussed the properties of neutral atoms and how they might be used in quantum computation. To facilitate the two-atom coupling necessary for computation, we saw how a strong dipole-dipole interaction is achieved by exciting atoms into the high-lying Rydberg state. This system was taken to create a realistic numerical model, capable of simulating experiment.

4

Efficient process characterisation

If a quantum system is subject to unitary and dissipative dynamics, it is a non-trivial task to theoretically determine the resulting process \mathcal{E} from a general input state to its corresponding output state. Solving that problem is highly relevant in quantum information science, as it quantifies not only the fidelity of gates for different input states but also the dominant error mechanisms. In turn this may eventually point to improved gates by appropriate control schemes. In this thesis we distinguish between (experimental) process tomography and (theoretical) characterisation of a process by solution of the master equation. A theoretical χ -matrix may be compared with experiments to validate interaction parameters [94, 95]. It may also be applied to investigate how errors accumulate when processes are applied to states, which are themselves the outcome of previous interactions (in a quantum algorithm for example).

This chapter will present a procedure to numerically determine the quantum

process \mathcal{E} from the master equation governing time-dependent system dynamics. Monte Carlo wave functions [48–50, 96] have allowed a numerically efficient alternative to the ordinary master equation approach to obtain the time dependent density matrix $\rho(t)$. Indeed, a Monte Carlo simulation of a quantum system with a Hilbert space of size D ($D \gg 1$) involves far less variables ($\sim D$) than its master equation counterpart ($\sim D^2$). In this chapter we simulate the evolution of our system from an initial maximally entangled state with a non-evolving ancilla system. We show that the Monte Carlo wave functions for this combined system can be directly processed to yield information about the quantum process \mathcal{E} .

This chapter is organized as follows. In section 4.1 we show how the time evolved Monte Carlo wave functions can be used to yield stochastic "process vectors" ζ that directly average to the process matrix χ . In section 4.2 we show how the no-jump, single wave function trajectory yields a readily accessible upper bound on the trace distance between the actual process matrix and any desired process matrix - a useful measure of process fidelity. In section 4.3 we apply our method to the simulation of a Rydberg blockade C_Z gate, subject to realistic decay and dephasing mechanisms. Section 4.5 concludes the chapter.

4.1 PROCESS CHARACTERISATION WITH MONTE CARLO

Since the outcome of a master equation evolution may be reproduced by state vectors in the Monte Carlo wave function method we have access to larger quantum systems. How this benefits process characterisation is the focus of this section. We first analyse ancilla assisted process characterisation using Monte Carlo wave functions (AAWF) and discuss its advantages over usual characterisation techniques. We conclude the section with a discussion of why the ancilla strategy is preferred over a Monte Carlo treatment of standard quantum process tomography.

We consider a bipartite wave function $|\Psi\rangle\rangle = \sum_r |r\rangle \otimes |r\rangle$ describing a principal system maximally entangled with an identical ancilla system. We subject the input state to a process $(\mathcal{E} \otimes \mathbb{1}) : |\Psi\rangle\rangle \rightarrow |\Psi_{\mathcal{E}}\rangle\rangle$, which acts on the principal system only ($\mathbb{1}$ is the identity operator). Picking the same set of Hermitian basis

operators $\{E_m\}$ as found in section 2.5, we may rewrite the action of this process in the following way

$$|\Psi_{\mathcal{E}}\rangle\rangle = \sum_m \zeta_m (E_m \otimes \mathbb{1}) |\Psi\rangle\rangle, \quad (4.1)$$

where ζ_m are elements of the ζ -vector.

Let $|j\rangle$ for $j \in \{1, \dots, D^2\}$ be the linearly independent basis for the space of D^2 -dimensional vectors on the principle-ancilla Hilbert space. We may catalogue the action of all operators $E_m \otimes \mathbb{1}$ on the bipartite input state as follows

$$(E_m \otimes \mathbb{1}) |\Psi\rangle\rangle = \sum_j \kappa_j^m |j\rangle. \quad (4.2)$$

where the $D^2 \times D^2$ matrix κ indexes these operations. The state resulting from the applied process, $|\Psi_{\mathcal{E}}\rangle\rangle$, may also be expanded onto $\{|j\rangle\}$

$$|\Psi_{\mathcal{E}}\rangle\rangle = \sum_j \lambda_j |j\rangle. \quad (4.3)$$

Combining Eqs. (4.1), (4.2) and (4.3) we obtain

$$\sum_m \kappa_j^m \zeta_m = \lambda_j, \quad (4.4)$$

which is the wave function analogue to Eq. (2.33).

Unlike the process matrix χ , determining the ζ -vector is not enough to characterise an open system. Realizing this, we take an ensemble of state vectors $|\Psi\rangle\rangle$ that evolve under the rules of Monte Carlo wave functions. Reintroducing the sum over the basis vectors $|j\rangle$ to both sides of Eq. (4.4), taking the outer product and averaging over the ensemble yields

$$\sum_{jk} \overline{\lambda_j \lambda_k^*} |j\rangle\langle k| = \sum_{jk, mn} \overline{\zeta_m \zeta_n^*} \kappa_j^m (\kappa_k^n)^* |j\rangle\langle k|, \quad (4.5)$$

because $\overline{\kappa_j^m(\kappa_k^n)^*} = \kappa_j^m(\kappa_k^n)^*$ - following from its definition in Eq. (4.2). By Eqs. (4.2) and (4.3) this may be rewritten as

$$\overline{|\Psi_{\mathcal{E}}\rangle\rangle\langle\langle\Psi_{\mathcal{E}}|} = \sum_{mn} \overline{\zeta_m \zeta_n^*} (E_m \otimes \mathbb{1}) |\Psi\rangle\rangle\langle\langle\Psi| (E_m^\dagger \otimes \mathbb{1}). \quad (4.6)$$

To progress, we refer to section 2.5 where the super operator $\mathcal{O} = \sum_{rs} \mathcal{O}_{rs} \otimes \mathcal{O}_{rs}$ was defined to represent all input matrices \mathcal{O}_{rs} necessary for process characterisation. Observe that \mathcal{O} is a pure state projection operator

$$\mathcal{O} = \sum_{rs} |rr\rangle\rangle\langle\langle ss| = |\Psi\rangle\rangle\langle\langle\Psi|. \quad (4.7)$$

Thus, the evolution of \mathcal{O} is equivalent to the propagation of $|\Psi\rangle\rangle \rightarrow |\Psi_{\mathcal{E}}\rangle\rangle$ under the rules of Monte Carlo wave functions. Equation (4.6) becomes

$$\mathcal{E}(\mathcal{O}_{rs}) \otimes \mathcal{O}_{rs} = \left[\sum_{mn} \overline{\zeta_m \zeta_n^*} (E_m \mathcal{O}_{mn} E_n^\dagger) \right] \otimes \mathcal{O}_{rs}, \quad (4.8)$$

from which we can conclude that

$$\chi_{mn} = \overline{\zeta_m \zeta_n^*}. \quad (4.9)$$

By averaging the ζ -vector coordinates over a sufficiently large ensemble of Monte Carlo wave functions we directly obtain the process matrix of Eq. (2.30).

Implementation of the AAWF method is described in Fig. 4.1.1. To propagate $|\Psi\rangle\rangle$ in a single Monte Carlo trajectory we must solve D coupled differential equations a total of D times. Thus, averaging over n trajectories requires solving $nD \times D$ coupled differential equations, which may be much less than the D^4 equations needed by standard techniques. Even more striking is the reduction in cost associated with the decomposition of κ , which scales as a $O(D^6)$ problem, compared to the $O(D^{12})$ decomposition problem associated with the \mathcal{K} -matrix of section 2.5.1. Each of the n Monte Carlo simulations at output creates a size $O(D^4)$ problem

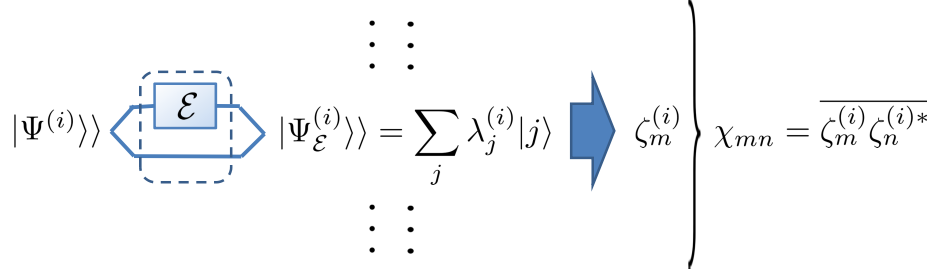


Figure 4.1.1: Implementation of ancilla assisted process characterisation with Monte Carlo wave functions: In each trajectory i , the evolution of the entangled principle-ancilla system is simulated, subject to the process $\mathcal{E} \otimes \mathbb{1}$. From the expansion coefficients $\lambda_j^{(i)}$, we determine the vector of components $\zeta_m^{(i)}$ (Eq. (4.4)). Averaging over many simulation outcomes $\zeta_m^{(i)} \zeta_n^{(i)*}$ the χ -matrix is obtained.

when using forward/backward substitution to solve for the ζ -vector.

In the spirit of standard process characterisation, we might have used Monte Carlo wave functions to simulate input states in the original Hilbert space, construct the output density matrices and subsequently solve for χ . However, for each of the D^2 input states we would have to simulate the trajectories of n Monte Carlo wave functions of size D , which is a larger problem than its AAPC counterpart (Table 4.1.1). Also, this method does not allow for a ζ -vector equivalent, meaning no reduction in the complexity of solving Eq. (2.33).

Note that the decomposition of \mathcal{K} is independent of the physical process \mathcal{E} , being entirely constructed from structural properties of the chosen operator and state bases of the quantum system. The same is true for the vector variant, applied to the analysis of Monte Carlo wave functions. Indeed, our vector formulation of the problem shows that the simpler decomposition of κ offers an effective reduction of the costs to decompose \mathcal{K} , which is applicable for standard process characterisation.

Table 4.1.1: Numerical cost of characterising a quantum process on a D dimensional Hilbert space. The first column lists the density matrix and Monte Carlo approaches to standard (SQPC) and ancilla assisted process characterisation (AAPC). The second column (c.d.e.) lists the number of coupled differential equations needed to simulate the time evolution. The last column (s.l.e.) lists the cost of solving the system of linear equations for the χ -matrix/ ζ -vector, assuming a Cholesky decomposition of the matrix \mathcal{K} (κ).

Technique	c.d.e.	s.l.e.
SQPC:		
density matrix	$D^2 \times D^2$	$O(D^8)$
Monte Carlo	$nD^2 \times D$	$O(D^8)$
AAPC:		
density matrix	$D^2 \times D^2$	$O(D^8)$
Monte Carlo	$nD \times D$	$n \times O(D^4)$

4.2 UPPER BOUND ERROR ESTIMATE FROM A SINGLE TRAJECTORY

We are interested in the characterisation of the effect of noise and dissipation on gate operations in quantum computing. To have any relevance for quantum computation such gates may only experience weak noise. This implies that in the majority of Monte Carlo simulations, the wave functions should follow the “no-jump” trajectory (2.15) through the entire duration of the process. Simulating this single wave function with the AAWF method provides a useful indication of the gate’s performance.

The simulated Monte Carlo wave functions making up a AAWF calculation of χ may be separated into two parts; those that never jumped, yielding a single ζ -vector and corresponding χ -matrix, $\chi_S = \zeta_S \zeta_S^\dagger$ and those that jumped at randomly assigned times to yield a set of vectors ($\chi_i = \zeta_i \zeta_i^\dagger$). The fraction $\frac{S}{n}$ of no-jump wave functions is equal to the product of the normalization factors $(1 - \delta p)$ in Eq. (2.15) applied over time. The remaining fraction $\frac{I}{n}$ of the simulated ensemble ($n = J + S$ being the total number of trajectories) yields the sum of terms $\chi_J = \frac{1}{J} \sum_{i=1}^J \zeta_i \zeta_i^\dagger$.

Finally we see that

$$\chi = \frac{S}{n}\chi_S + \frac{J}{n}\chi_J. \quad (4.10)$$

The trace distance measure is a metric on the space of quantum states and serves as a simple quantitative measure between them. It is defined by $T(A, B) \equiv \frac{1}{2}\|A - B\|_{tr}$, where $\|C\|_{tr} = \text{Tr}(\sqrt{C^\dagger C})$ is the trace norm. Calculating the trace distance between Eq. (4.10) and the ideal process matrix $\tilde{\chi}$ we employ the triangle inequality and translational invariance to obtain

$$T(\tilde{\chi}, \frac{S}{n}\chi_S + \frac{J}{n}\chi_J) \leq T(\tilde{\chi} - \frac{S}{n}\chi_S, 0) + T(0, \frac{J}{n}\chi_J). \quad (4.11)$$

Since $T(0, \frac{J}{n}\chi_J) = \frac{1}{2}\|\frac{J}{n}\chi_J\|_{tr} = \frac{J}{2n}$, this provides an upper bound on the trace distance using the evolution of only a single no-jump wave functions and its associated χ matrix,

$$T(\tilde{\chi}, \chi_S + \chi_J) \leq T(\tilde{\chi}, \frac{S}{n}\chi_S) + \frac{J}{2n}. \quad (4.12)$$

Clearly, this upper bound is of limited value if dissipation is significant and many wave functions jump.

Another typical measure for the effect of error in a process is fidelity, defined by $F(\tilde{\chi}, \chi) \equiv \|\sqrt{\tilde{\chi}}\sqrt{\chi}\|_{tr}$. However, being a non-linear expression it has a more complicated relation with the different components of the wave function ensemble. We shall return to both process error measures in the numerical example below.

4.3 RYDBERG MEDIATED CONTROLLED-Z GATE

As an example of our process characterisation, we consider the controlled-Z (C_Z) gate operation between atoms coupled by the Rydberg blockade interaction (Fig. 4.3.1). Each atom has four levels; two ground levels which comprise the qubit space, the Rydberg level with which the atoms interact, and the intermediate level which facilitates transitions to the Rydberg level via a two-photon process. Thus, even though the initial state space and resulting process matrix may be restricted to the qubit space we are still required to simulate the system considering all levels.

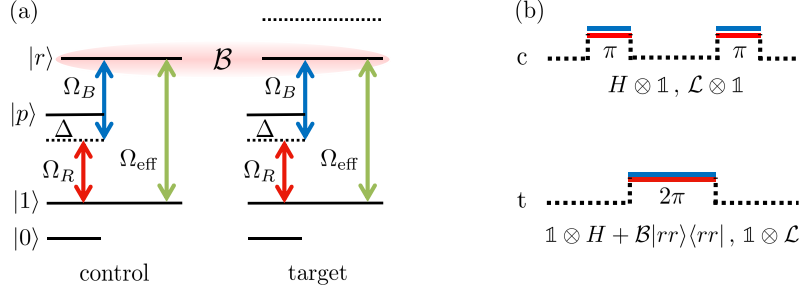


Figure 4.3.1: Rydberg mediated controlled-Z gate. (a) Level structure of a Rydberg atom. This includes the qubit states $|0\rangle$ and $|1\rangle$, intermediate state $|p\rangle$ and Rydberg state $|r\rangle$. Resonant transfer from $|1\rangle$ to $|r\rangle$ is achieved by a two photon process via $|p\rangle$. The red (blue) laser coupling $|1\rangle$ ($|r\rangle$) to $|p\rangle$ at Rabi frequency Ω_R is detuned from $|p\rangle$ by frequency Δ . By eliminating the intermediate state we arrive at an effective Hamiltonian that describes a $|0\rangle \rightarrow |r\rangle$ transition at Rabi frequency $\Omega_{\text{eff}} = \Omega_R \Omega_B / 2\Delta$. When two such atoms are in close proximity ($\sim 10 \mu\text{m}$) a control atom in the Rydberg state will block resonant transfer of any other (target) atom into $|r\rangle$ because of the Rydberg-Rydberg interaction energy shift \mathcal{B} . (b) Depicts the pulse sequence of a C_Z gate. The pulses are “square”, meaning the Hamiltonian has no time dependence within any given pulse. The operator H is the effective Hamiltonian and $\mathbb{1}$ represents the identity operation on the target (top) and control (bottom) atom. The operator $\mathcal{L} = -\frac{i}{2} \sum_m L_m^\dagger L_m$ describes decoherence in the system and the two-atom interaction $\mathcal{B}|rr\rangle\langle rr|$ prevents both atoms from occupying the Rydberg state.

Obtaining the χ -matrix even for the simplest two-qubit gates is non-trivial, and extending it beyond two atoms becomes computationally challenging for standard characterisation strategies. Meanwhile, the proposed AAWF method can readily deal with multi-qubit process characterisation involving up to 8-10 atoms.

An controlled-Z gate performs a Pauli-Z operation on a target atom depending on the state of a control atom. An ideal Rydberg mediated C_Z gate is achieved through excitation to the high-lying Rydberg state $|r\rangle$. The qubit state $|1\rangle$ of both the control (c) and target (t) atom are coupled to $|r\rangle$. If the control atom is excited to $|r\rangle$ in the first π -pulse, it shifts the energy of the target’s Rydberg state by the blockade frequency \mathcal{B} . Unless both atoms start in the qubit $|0\rangle$ state and assuming perfect blockade, the two-atom state will pick up a π phase shift upon completion

Table 4.3.1: Physical parameters for our simulations based on values discussed in Refs. [91, 97].

Experimental parameter	Symbol	Value
Detuning	$\Delta/2\pi$	2.0 GHz
Red Rabi frequency	$\Omega_R/2\pi$	118 MHz
Blue Rabi frequency	$\Omega_B/2\pi$	10 - 130 MHz
Rydberg blockade	$\mathcal{B}/2\pi$	20 MHz
Decay rate ($ p\rangle$)	$\gamma_p/2\pi$	6.07 MHz
Decay rate ($ r\rangle$)	$\gamma_r/2\pi$	0.53 kHz
Dephasing rate ($ r\rangle$)	$\gamma_d/2\pi$	1.0/2.0 kHz

of the pulse sequence.

A C_Z gate on the $5s_{1/2}$ hyperfine states $|0\rangle \equiv |F = 1, m_F = 0\rangle$ and $|1\rangle \equiv |F = 2, m_F = 0\rangle$ involves single qubit rotations between $|1\rangle$ and the Rydberg state $|r\rangle = |97d_{5/2}, m_j = 5/2\rangle$. This is a two photon process, achieved with σ_+ polarized 780- and 480-nm beams. The 780-nm beam is tuned by Δ to the red of the $|1\rangle \rightarrow |p\rangle \equiv |5p_{3/2}, F = 3\rangle$ transition while the 480-nm beam is blue detuned from $|p\rangle$ by Δ . The resulting Rabi frequencies are Ω_R (Ω_B) for the red (blue) detuned laser. After adiabatically eliminating $|p\rangle$ from the system, the effective Hamiltonian describing Rydberg rotations is (section 3.4.1)

$$H = \underbrace{\frac{(2\Delta - \delta E_r)\Omega_R\Omega_B}{8\Delta(\Delta - \delta E_r) + 2\gamma^2}}_{\Omega_{\text{eff}}/2} |1\rangle\langle r| + \text{H.c.}, \quad (4.13)$$

where the coefficient of $|1\rangle\langle r|$ is half of the effective Rabi frequency Ω_{eff} , the offset δE_r may be approximated by $\sqrt{\Omega_R^2 - \Omega_B^2}$ and H.c. denotes Hermitian conjugate.

Decay from $|p\rangle$, at the rate γ , may be recast into effective form

$$L_{\gamma_p, j} = \frac{\sqrt{c_j\gamma_p}\Omega_R}{2\Delta - i\gamma} |j\rangle\langle 1| + \frac{\sqrt{c_j\gamma_p}\Omega_B}{2(\Delta - \delta E_r) - i\gamma} |j\rangle\langle r|, \quad (4.14)$$

where c_i are the branching ratios for decay from $|p\rangle$ into $|0\rangle$ ($c_0 = 0.32$), $|1\rangle$ ($c_1 = 0.12$) and the “loss state” $|g\rangle$ ($c_g = 0.56$). The loss state cannot be ignored in simulation as it features heavily in the decay from $|p\rangle$. We remember that it may be omitted from the system’s Hamiltonian by disposing a Monte Carlo trajectory that simulates an atom loss. Its contribution to the processes overall error is calculated by counting the number of discarded trajectories. Dephasing due to magnetic field noise and atomic motion are described by

$$L_{\gamma_d} = \sqrt{\gamma_d}(\mathbb{1} - 2|r\rangle\langle r|), \quad (4.15)$$

where $\mathbb{1}$ is shorthand for the identity operator. Spontaneous emission from $|r\rangle$, described by the jump operator

$$L_{\gamma_r} = \sqrt{\gamma_r}|p\rangle\langle r|, \quad (4.16)$$

temporarily populates the eliminated state $|p\rangle$ before jumping to one of the lower lying states. This system is discussed further in Sec. 3.4. Parameters chosen in simulation are listed in Table 4.3.1.

4.3.1 PROCESS CHARACTERISATION

Ideally an characterisation of a C_Z gate due to an experimental realization, and thus numerical simulation, should reproduce the χ -matrix depicted in Fig. 4.3.2. It usually doesn’t and in Fig. 4.3.3(a) we show the trace distance between the ideal process matrix $\tilde{\chi}$ and one simulated with decohering processes χ , plotted as a function of the blue laser Rabi frequency Ω_B . There are three sets of solid and dashed lines, these are separate calculations based on the size of the blockade shift.

The solid curves are based on our simulations with ensembles of $n = 500$ Monte Carlo wave functions. There are two physical considerations that determine the optimum blue Rabi frequency seen in Fig. 4.3.3(a). Gate time $t_{\text{gate}} \propto 1/\Omega_{\text{eff}}$ lengthens as Ω_B decreases, allowing greater opportunity for error from in-

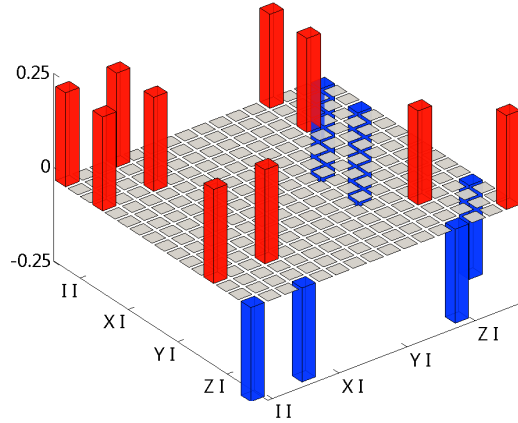


Figure 4.3.2: Real part of the process matrix characterising the ideal (no decohering processes) controlled-Z gate. Sub-tick labels to the right of each $\mathcal{W}I$ read $\mathcal{W}X, \mathcal{W}Y, \mathcal{W}Z$, where $\mathcal{W} \in \{I, X, Y, Z\}$.

intermediate state decay and dephasing. As the effective Rabi frequency matches and then exceeds \mathcal{B} the blockade becomes ineffective and population from the target atom rotates through the Rydberg state, thereby picking up an unwanted phase. We find an optimum between these two regimes and, although certain to pose experimental challenges, there is a clear advantage by working with larger blockade frequencies. We note that these results differ slightly from the analysis in section 3.2.2, where it was shown that an optimal Rabi frequency was found by balancing the blockade strength against the Rydberg state lifetime. Decay from the Rydberg state was included in the simulation but dephasing was seen to be the leading source of error.

The dashed curves are upper bound calculations using a single no-jump trajectory (cf. Sec. 4.2). It can be clearly seen that they exceed the corresponding Monte Carlo simulation, confirming the validity of this approach. If only a rough measure or trend over a range of parameters is needed, this tool offers a drastic speed-up over conventional methods. It is interesting to note that the upper bound results converge to that of the Monte Carlo calculations as the Rabi frequency increases. We remember that the quality of the upper bound depends on the number of quan-

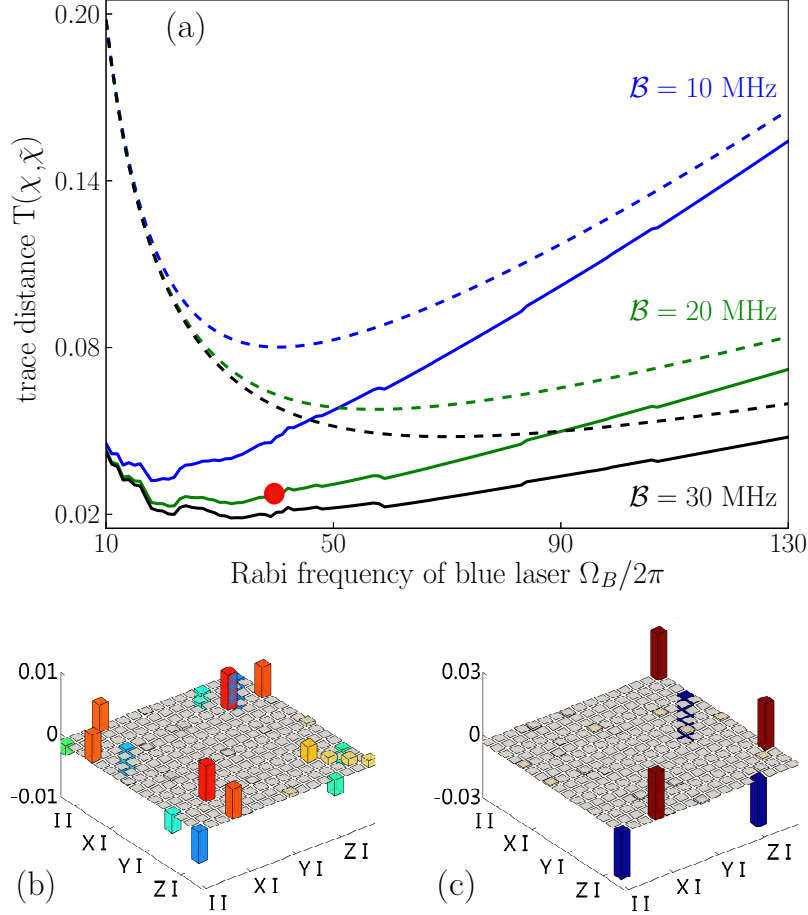


Figure 4.3.3: Simulating the χ -matrix with AAWF. (a) Trace distance as a function of the blue laser Rabi frequency for three experimental realizations of blockade strength. Shown is full AAWF treatment (solid line) and “no-jump wave function” upper bound (dotted line). Parameters are listed in Table 4.3.1 using $\gamma_d/2\pi = 1.0$ kHz. (b) Real and (c) imaginary part of the difference between the ideal and simulated process matrix for a C_Z gate [N.B. Sub-tick labels to the right of each $\mathcal{W}I$ read $\mathcal{W}X, \mathcal{W}Y, \mathcal{W}Z$, where $\mathcal{W} \in \{I, X, Y, Z\}$]. Parameters are that of (a) but choosing $\Omega_B = 40$ MHz, indicated by the (red) dot.

tum “jumps”. In quantum computation it is usually assumed (or hoped) that there are not many. A larger Rabi frequency translates into a shorter gate time and thus less opportunity for jumps.

Figures 4.3.3(b) and 4.3.3(c) illustrate the difference between the process matrix elements of an ideal C_Z gate and one simulated with decoherence. We note that this is a characterisation of the qubit states only. Although the Rydberg state was involved in simulation it is only a mediating state, quantum information is stored on the qubit states. These figures serve as a reminder that although the trace distance offers a good quantitative measure we have access to more information through a complete process characterisation.

4.4 ERROR ANALYSIS

The Monte Carlo wave functions on average yield the density matrix. This is true for any ensemble size, while the statistical errors on the estimate decrease with increasing n . The trace distance and the fidelity measures are not linear functions in the density matrix elements. Hence, sampling their values with a finite wave function ensemble may provide a systematic error in addition to the statistic uncertainty of the method. In [98], a non-linear master equation was analysed and the systematic error was estimated to scale as $1/n$, becoming less important than the statistical error ($\sim 1/\sqrt{n}$) for large ensembles. Convergence of the AAWF method is illustrated in Fig. 4.4.1, where trace distance $T(\tilde{\chi}, \chi)$ and fidelity $F(\tilde{\chi}, \chi)$ are recorded for different Monte Carlo wave function ensemble sizes. For each ensemble size, we have made 50 simulations and at $n = 500$, sample-to-sample variations are small enough to consider the output results satisfactorily converged.

4.5 DISCUSSION AND CONCLUSION

In conclusion we have presented a numerically efficient method to obtain the χ -matrix for an arbitrary quantum process from a solution to the system’s master

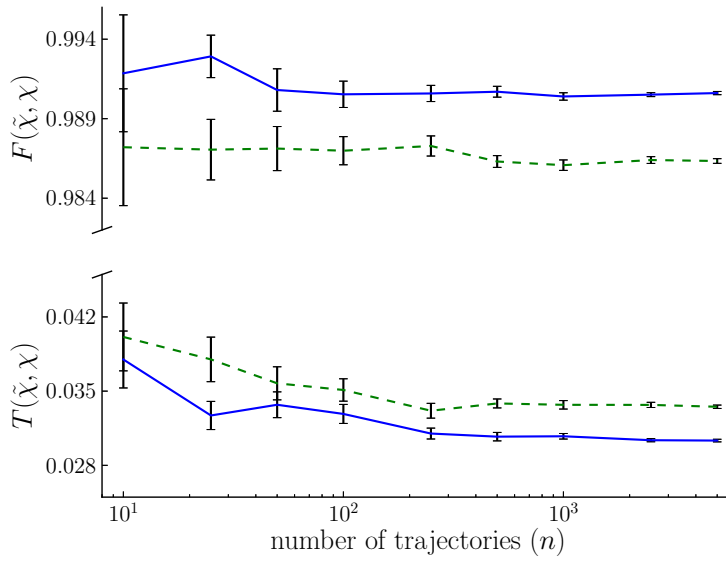


Figure 4.4.1: Convergence of the process fidelity and trace distance determined by the ancilla assisted wave function characterisation method. For selected values of n the mean value and standard deviation of the fidelity (top) and trace-distance (bottom) is obtained using 50 samples. Each sample involves a process matrix simulation with n trajectories. The solid lines represent calculations using the parameters in Table 4.3.1 with $\gamma_d/2\pi = 1.0$ kHz. The dashed lines are obtained with the higher dephasing rate $\gamma_d/2\pi = 2.0$ kHz.

equation. Monte Carlo wave functions present an effective means to simulate the system density matrix and extends in a natural way to model ancilla assisted process characterisation. Parametrizing the outcomes of the simulated system under a fixed set of operations we presented a ζ -vector representation of the Monte Carlo wave functions. Because the process matrix χ results as a simple product of ζ -vector components the numerical effort to both simulate state evolution and represent the process adequately were significantly reduced. We also showed why this method is preferred over a straightforward retrieval of output density matrices from averaged wave function components. The Monte Carlo wave function method provides the further insight that, in the case of little dissipation, a single “no-jump” trajectory is enough to find an upper bound on trace distance between the ideal χ and the simulated one. Such upper bound estimates may be helpful in estimating optimal parameters for experiments. Furthermore, our analysis showed that the mathematical inversion problem occurring in standard process characterisation can be solved in the much lower dimensional vector space. Although identified by our state vector formalism, it may be applied to density matrices in usual process tomography. A demonstration on the Rydberg mediated two-qubit controlled-Z gate showed proof-of-principle calculations that the method is capable of efficiently modelling a quantum computing implementation based on neutral atoms.

5

Error accumulation in quantum circuits

Since the first proposals were made to use quantum effects for computing purposes there has been a strong focus on how errors and imperfections may harm and even prevent successful application of quantum computing. A simple estimate suggests that if each single operation in a computation entails an error with a probability $p > 0$ then the application of k operations will lead to a useful outcome with a probability that decreases exponentially $\sim (1 - p)^k$. Error correction codes have provided a way to correct these errors up to a certain probability threshold, thereby allowing scalable fault-tolerant quantum computing [28, 99].

The error occurring in a single computational step such as a one- or two-qubit gate is often characterised by a single number (i.e. trace distance), typically related to the overlap between the desired and actual output state, averaged over all input states. However, there is no guarantee that such a number encapsulates the accumulation of errors in a quantum circuit where the output state of one opera-

tion serves as the input to the next. Errors may build up coherently, so that error probabilities grow quadratically rather than linearly with time, or so that they compensate each other, cf., bang-bang control and composite pulses [100–102]. Thus, a concatenation of two imperfect gates can lead to either unusable results or a correcting mechanism. To theoretically characterise a complete quantum circuit is a formidable task and is ultimately at odds with using a physical system to solve computationally hard problems. Still, a theoretical analysis of how errors propagate and accumulate in small systems may guide efforts to pick among different implementations of gates and assess optimal strategies for error correction.

In this chapter, processes in a quantum system are described by χ -matrices. In quantum computing we aim to implement definite gate operations and process matrices account for the effects of error, e.g., due to dissipation and decoherence. It will be shown how χ -matrices calculated once for one- and two-qubit gates can be concatenated to characterise circuits built from many of these gates. This will be exemplified in neutral atom quantum computing where the Rydberg blockade mechanism is used for two-qubit quantum gates [63, 74]. Circuits comprised of Rydberg mediated two-qubit gates may be directly compared to alternative multi-qubit implementations exploiting a single Rydberg atom’s ability to simultaneously control a number of neighbouring atoms.

The chapter is organized as follows. In section 5.1, we outline the definition of χ -matrices and how they may be computed with Monte Carlo wave function simulations. In section 5.2, we describe how χ -matrices for simple processes on few particles are concatenated to characterise large quantum circuits. In section 5.3, we briefly reiterate the Rydberg blockade gate scheme for completeness. In section 5.4, we concatenate one- and two-qubit gate χ -matrices in a neutral atom system to characterise the circuit performing a Toffoli gate. This we compare to a direct multi-atom Rydberg mediated implementation. In section 5.5, we conclude.

5.1 PROCESS MATRIX IDENTIFICATION

Consider the action of a quantum process that takes an input density matrix ρ describing a physical system with Hilbert space dimension D to an output density matrix. We remember that such a process, described as a completely-positive linear map $\mathcal{E} : \rho \rightarrow \mathcal{E}(\rho)$, may be written (section 2.5),

$$\mathcal{E}(\rho) = \sum_{mn} \chi_{mn} E_m \rho E_n^\dagger, \quad (5.1)$$

by introducing a complete basis of D^2 operators $\{E_n\}$ on the Hilbert space. The $D^2 \times D^2$ elements χ_{mn} constitute the process matrix χ .

If the system is subject to known dissipation and decoherence mechanisms, the quantum system evolution may be modelled theoretically and the process matrix be calculated by solution of the quantum master equation. A gate operation typically involves application of time dependent laser pulses. Therefore, it is valuable to determine how losses and errors accumulate and contribute to different types of errors in the output. Such detailed studies may also serve to confirm the values of experimental parameters [94, 95].

We saw in chapter 4 that quantum processes may be characterised using an ensemble of Monte Carlo wave functions. There are a number of reasons that make it desirable in this chapter, which finds χ for (large) quantum circuits: First, for large D , an adequate ensemble of wave functions is easier to store and evolve than density matrices. Second, obtaining χ through the output state data from an ensemble of wave functions is less costly, numerically, than from a density matrix. Third, the stochastic evolution consists of a deterministic smooth evolution interrupted by “quantum jumps”. If only an estimate is needed, a single deterministic “no-jump” wave function suffices to provide a rigorous bound on the process matrices describing the evolution.

5.2 THE PROCESS MATRIX FOR A QUANTUM CIRCUIT

Suppose the quantum circuit performing a computational task is composed of N physical units. The Hilbert space of the entire system is then a tensor product of N Hilbert spaces, each of dimension d . An implementation of a quantum process often requires using more than just the qubit states. However, since the physical units only process binary information we shall refer to them as qubits, even if we exploit states from a space larger than dimension 2. On each qubit Hilbert space we assume the complete operator basis $\{e_{n_i}\}$. By merely forming tensor products of the basis operators, we obtain a complete operator basis $\{E_n = e_{n_1} \otimes \dots \otimes e_{n_N}\}$ for the N qubits, where the single index n represents all values of the set n_1, \dots, n_N .

If we assume that (i) process matrices χ correctly describe processes acting separately on one and two qubits of the circuit, and (ii) the decay and dissipation is independent and uncorrelated on different particles and at different times (no super-radiance or non-Markovian effects) then the application of several one- and two-qubit operations is exactly represented by an appropriate concatenation of the corresponding process matrices. The operator tensor product structure provides a convenient representation of the operators E_m (E_n^\dagger) in Eq. (5.1) and enables a straightforward calculation of the $D^2 \times D^2 = d^{2N} \times d^{2N}$ dimensional process matrices χ for multi-qubit processes.

5.2.1 PARALLEL CONCATENATION

Suppose two subsystems are simultaneously subjected to processes independent of each other. These processes, $\mathcal{E}^{(1)}$ and $\mathcal{E}^{(2)}$, may be described by the process matrices $\chi^{(1)}$ and $\chi^{(2)}$ respectively, illustrated as two- and one-qubit gates in Fig. 5.2.1(a). The combined three-qubit process matrix $\chi^{(1,2)}$ is simply the tensor product of the independent χ matrices. Other systems may be present but idle during the gate operation. They are acted on by the identity operator in the process matrix tensor product.

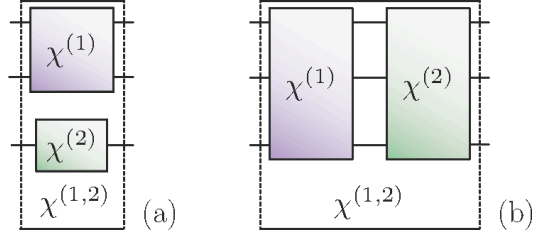


Figure 5.2.1: Parallel and serial concatenation: Concatenation of (a) processes acting simultaneously on different qubits, and (b) processes acting sequentially on the same set of qubits. Expressions for the resulting process matrices $\chi^{(1,2)}$ are discussed in the text.

5.2.2 SERIAL CONCATENATION

Most quantum algorithms make use of many computational steps, where the output of every step serves as the input to the subsequent one. In Fig. 5.2.1(b) we illustrate this situation for two consecutive three-qubit operations $\mathcal{E}^{(1)}$ and $\mathcal{E}^{(2)}$ characterised by $\chi^{(1)}$ and $\chi^{(2)}$ respectively. If the output $\mathcal{E}^{(1)}(\rho)$ of the input density matrix ρ becomes the input of $\mathcal{E}^{(2)}$, what is the resulting χ matrix? Formally, the output of the sequential application of the operations is given by

$$\mathcal{E}^{(2)}(\mathcal{E}^{(1)}(\rho)) = \sum_{pq} \chi_{pq}^{(2)} E_p \left(\sum_{mn} \chi_{mn}^{(1)} E_m \rho E_n^\dagger \right) E_q^\dagger, \quad (5.2)$$

Since the operators E_r form a complete set, any product $E_p E_m$ can be expanded on these operators, that is, $E_p E_m = \sum_{rp} c_{pm}^r E_r$ and $E_n^\dagger E_q^\dagger = \sum_{nq} (c_{qn}^s)^* E_s^\dagger$. Equation (5.2) then becomes

$$\mathcal{E}^{(2)}(\mathcal{E}^{(1)}(\rho)) = \sum_{rs} \chi_{rs}^{(1,2)} E_r \rho E_s^\dagger, \quad (5.3)$$

where

$$\chi_{rs}^{(1,2)} = \sum_{mn,pq} c_{pm}^r \chi_{mn}^{(1)} \chi_{pq}^{(2)} (c_{qn}^s)^*. \quad (5.4)$$

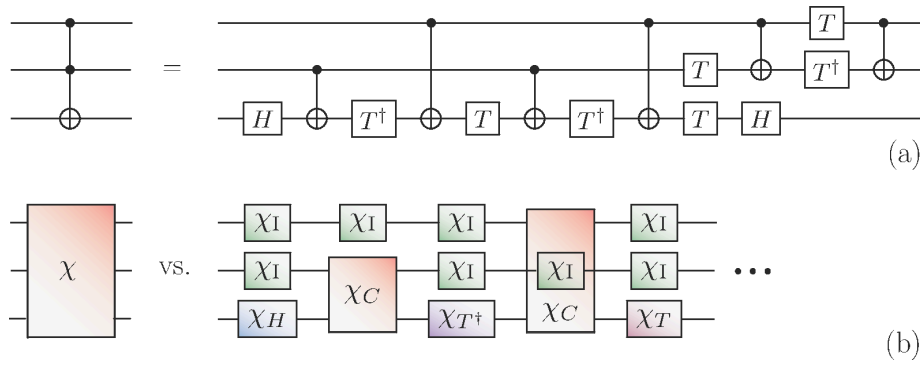


Figure 5.2.2: The Toffoli gate: (a) The three-qubit Toffoli gate on the left may be reproduced by a circuit of CNOT, Hadamard (H), $T = \exp(i\pi\sigma_z/8)$ and T^\dagger gates, shown to the right. (b) The process matrix χ (left), characterising the Toffoli gate may be calculated by concatenation of one- and two-qubit process matrices (right). The process matrices χ_C , χ_H , χ_T and χ_{T^\dagger} characterise the CNOT, Hadamard, T and T^\dagger gates respectively. The “identity” process matrix χ_I indicates an idle qubit.

Note that although two consecutive processes may act on different subsets of some multi-qubit system, both operations may be reformulated to act on the entire system through parallel concatenation.

It now becomes apparent that once the process matrices of all contributing gates in a circuit have been computed conclusively, we limit the cost of finding $\chi^{(1,2)}$ and thus of process matrices for larger quantum circuits. The assessment of how errors accumulate becomes a function of the width and depth of the quantum circuit.

5.2.3 EXAMPLE: TOFFOLI GATE

The Toffoli gate, or C_2 NOT gate, performs the NOT operation on a target qubit depending on the state of two control qubits. The Toffoli gate may be implemented as a sequence of six two-qubit CNOT gates and nine one-qubit Hadamard, $T = \exp(i\pi\sigma_z/8)$ and T^\dagger phase gates, see Fig.5.2.2(a). The gate and its generalization to higher numbers of control qubits (C_k NOT) have applications as sub-modules in different quantum computing algorithms. Thus, it is relevant to determine the

process matrix for its implementation in realistic systems.

In the analysis of the Toffoli gate process matrix we first simulated the propagation of quantum states through the sequence of one- and two-qubit gates in the full three-qubit Hilbert space. Such a calculation, e.g. using Monte Carlo wave functions to include dissipation, yields the full circuit process matrix χ_{cir} . Next, assuming the independence of errors occurring on different qubits and in different gates we apply the concatenation rules to obtain the circuit's process matrix χ_{cat} . Its repeated use of the same CNOT χ matrix (cf. Fig. 5.2.2(b)), which only needs a single calculation on a two-qubit system, attests to the advantage of the latter approach.

5.3 RYDBERG BLOCKADE QUANTUM GATES

In Rubidium, a convenient choice for the qubit states are the hyperfine ground states $|0\rangle \equiv |5s_{1/2}, F = 1, m_F = 0\rangle$ and $|1\rangle \equiv |5s_{1/2}, F = 2, m_F = 0\rangle$. They can be selectively excited to the Rydberg state $|r\rangle = |97d_{5/2}, m_j = 5/2\rangle$ by a two photon process using a 780-nm (480-nm) laser field, tuned by an amount Δ to the red (blue) of the intermediate $|p\rangle \equiv |5p_{3/2}, F = 3\rangle$ state. The Rabi frequency associated with the red (blue) detuned laser is Ω_R (Ω_B), illustrated in Fig. 5.3.1(a). An atom that achieves excitation to the Rydberg state shifts the $|r\rangle$ state energy of all other atoms within the so-called blockade radius by an amount \mathcal{B} . Thus, one excited atom can prevent the resonant excitation of its neighbouring atoms and this is the basis for effective quantum gates between them.

Dephasing of the Rydberg level normally associated with magnetic field noise and atomic motion is modeled by the operator $L_{\gamma_d} = \sqrt{\gamma_d}(\mathbb{1} - 2|r\rangle\langle r|)$, where γ_d is the dephasing rate and $\mathbb{1}$ is shorthand for the identity operator. Spontaneous decay from a state $|y\rangle$ to a lower lying state $|z\rangle$ at a rate γ_y is modelled by the jump operator $L_{\gamma_y} = \sqrt{\gamma_y}|z\rangle\langle y|$. The effects of both dissipation mechanisms are simulated using the Monte Carlo wave function method (section 2.3). Characteristic parameters are summarized in Table 5.3.1.

Table 5.3.1: Physical parameters for our simulations based on values discussed in Refs. [91, 97].

Experimental parameter	Symbol	Value
Detuning	$\Delta/2\pi$	2.0 GHz
Red Rabi frequency	$\Omega_R/2\pi$	118 MHz
Blue Rabi frequency	$\Omega_B/2\pi$	10 - 100 MHz
Rydberg blockade	$\mathcal{B}/2\pi$	20 MHz
Decay rate of $ p\rangle$	$\gamma_p/2\pi$	6.07 MHz
Decay rate of $ r\rangle$	$\gamma_r/2\pi$	0.53 kHz
Dephasing rate of $ r\rangle$	$\gamma_d/2\pi$	1.0 kHz

Adiabatic elimination by the effective operator formalism detailed in section 3.4 provides a mechanism to decouple the intermediate optically excited state and describe the coherent and incoherent dynamics within the subspace of $|0\rangle$, $|1\rangle$ and $|r\rangle$. The system is then described by a Hamiltonian coupling a selected qubit state to $|r\rangle$ by an effective Rabi frequency. We remember that the formalism also provides an effective form for the operators describing decohering processes.

5.3.1 RYDBERG BLOCKADE CNOT GATE

In atomic quantum computing proposals single qubit gates amount to fast, resonant transitions within single atoms and can be made with high precision. Thus, for the purpose of this study we assume that the χ matrices associated with one-qubit gates are identical to the desired ones. The two-qubit CNOT gate depends on finite interactions between excited state atoms, lengthening gate time and making it prone to dissipation and decoherence. The process matrix of an ideal CNOT gate is illustrated in Fig 5.3.2.

Figure 5.3.1(b) illustrates how a unitary CNOT gate between two atoms can be implemented by a sequence of five perfect π -pulses. First, (pulse 1) transferring the control qubit's population from $|0_c\rangle$ to $|r_c\rangle$, then (pulses 2-4) transferring the target qubit's population between $|0_t\rangle$ and $|1_t\rangle$ via the state $|r_t\rangle$ and finally (pulse

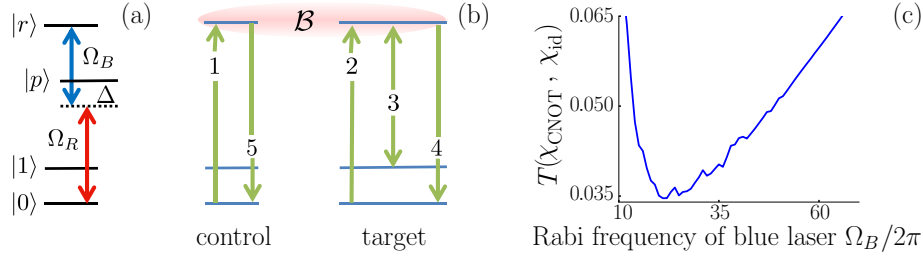


Figure 5.3.1: Simulation and characterisation of the controlled-NOT gate: (a) The red (lower) and blue (upper) laser fields drive $|0\rangle$, via $|p\rangle$, into the Rydberg state $|r\rangle$ by two-photon absorption. (b) Implementation of the CNOT gate involves a sequence of two-photon π -pulses: (pulse 1) the control atom makes the transition $|0\rangle$ to $|r\rangle$. The target atom then makes the transitions, (pulse 2) $|0\rangle \leftrightarrow |r\rangle$, (pulse 3) $|1\rangle \leftrightarrow |r\rangle$ and (pulse 4) $|0\rangle \leftrightarrow |r\rangle$. In pulses 2-4 the target atom's states $|0\rangle$ and $|1\rangle$ are swapped, but only if the control atom is not in $|r\rangle$. Finally, (pulse 5) the control atom is driven from $|r\rangle$ back to $|0\rangle$. (c) Trace distance (see text in Sec. 5.3A) between the ideal CNOT process matrix and the process matrix calculated for the implementation shown in panel (b), with the parameters listed in Table 4.3.1. The trace distance is shown as a function of the blue laser Rabi frequency Ω_B .

5) returning the control qubit's population from $|r_c\rangle$ to $|0_c\rangle$. If the control qubit initially populates the state $|0_c\rangle$ the Rydberg blockade prevents any transfer during pulses 2-4. Thus, a NOT operation on the target qubit is conditioned on the control qubit initially populating the state $|1_c\rangle$, defining it to be a CNOT operation.

Monte Carlo wave functions were used to simulate the five π -pulse implementation of the CNOT gate (Fig. 5.3.1) with the parameters of Table 5.3.1. The performance of the gate was investigated as a function of the blue laser Rabi frequency Ω_B . To provide a simple quantitative measure we applied the trace distance measure $T(\chi_{\text{sim}}, \chi_{\text{id}})$ between the simulated and ideal process matrix, where $T(A, B) \equiv \frac{1}{2} \|A - B\|_{tr}$ and $\|C\|_{tr} = \text{Tr}(\sqrt{C^\dagger C})$ is the trace norm. Note that this distance measure is less “forgiving” than, for example, measures based on the trace overlap [94]. In Fig. 5.3.1(c) we show trace distance between a simulated CNOT gate process matrix and the ideal unitary process matrix. At low values of Ω_B the gate experiences greater dephasing errors from population in the Rydberg state, due to

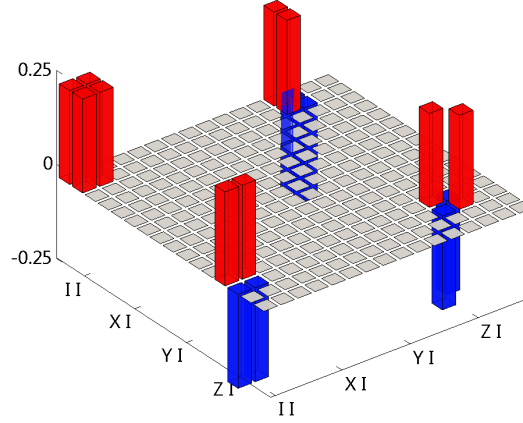


Figure 5.3.2: Real part of the process matrix characterising the ideal controlled-NOT gate. Sub-tick labels to the right of each $\mathcal{W}I$ read $\mathcal{W}X, \mathcal{W}Y, \mathcal{W}Z$, where $\mathcal{W} \in \{I, X, Y, Z\}$.

long gate times. At large Ω_B the blockade mechanism becomes inefficient. Thus, the optimum Rabi frequency lies between these two regimes.

5.4 THE TOFFOLI GATE BY RYDBERG BLOCKADE

We demonstrate the characterisation of the Toffoli gate resulting from simulation in Fig. 5.4.1. The process matrix χ_{cat} of the Toffoli gate in the circuit implementation (Fig. 5.2.2) may be obtained without further simulation by a concatenation of the single qubit process matrices and the CNOT process matrix of Sec. 5.3A. Alternatively, we may simulate the circuit implementation in the full three-qubit Hilbert space to obtain χ_{cir} . In the simulation of a Rydberg mediated gate, the characterisation of a single qubit has a Hilbert space dimension of $d = 4^2$, which translates into a 4^6 problem for the three qubit circuit characterisation.

The top dashed (solid) curve in Fig. 5.4.1 illustrates trace distance between the full circuit χ_{cir} (concatenated χ_{cat}) process matrix to the ideal process matrix χ_{id} , plotted as a function of Ω_B . Each point in both curves is determined by propagating 500 wave function trajectories. The discrepancy between the two curves is due to χ_{cat} , which makes use of the same simulated CNOT process matrix several

times. Concatenating the process matrices of the same CNOT simulation also “concatenates” the error associated with the simulation. The total error grows (non-linearly) with the number of gates. This is demonstrated in Fig. 5.4.1, where the discrepancy between the curves depends on Ω_B . For lower values of Ω_B , and thus slower gate operation, gate error is dominated by (non-unitary) processes such as dephasing. As correct Monte Carlo wave function statistics are sensitive to non-unitary errors, we find at small Ω_B the relatively large discrepancy between $\text{Tr}(\chi_{\text{cat}}, \chi_{\text{id}})$ and $\text{Tr}(\chi_{\text{cir}}, \chi_{\text{id}})$ to be expected at slow gate speeds (see Ref. [98] for an analysis of a similar situation). This is in contrast to results at high values of Ω_B , where gate error is unitary and caused by an imperfect blockade. The discrepancy between $\text{Tr}(\chi_{\text{cat}}, \chi_{\text{id}})$ and $\text{Tr}(\chi_{\text{cir}}, \chi_{\text{id}})$ vanishes as Ω_B increases. We note that the Toffoli gate consists of six CNOT gates and the trace distance to the ideal gate is, indeed, roughly six times the one shown in Fig. 5.3.1(c).

A Rydberg excited atom blocks excitation of any number of atoms within the Rydberg interaction blockade radius, which may be of order $10 \mu\text{m}$. Thus, it is possible to contain an entire qubit register within a single blockade radius, allowing implementation of multi-qubit gate operations which are faster than the circuit equivalent [103]. One such protocol is the $C_k\text{NOT}$ gate operation, illustrated in Fig. 5.4.2 [86].

For $k = 2$ the gate becomes the Toffoli gate and calculation of the χ -matrix is only possible by simulating the complete three-qubit register. The trace distance between the process matrix resulting from simulation and the ideal process matrix is shown as the lower black curve in Fig. 5.4.1. Remarkably, the multi-qubit implementation, with interactions allowed between all three atoms, performs markedly better than the Toffoli circuit consisting of one- and two-qubit operations. In comparison with the CNOT gate, the minimal trace distance here is approximately 1.5 times larger. This is consistent with using 7 π -pulses rather than the 5 needed for a single CNOT gate.

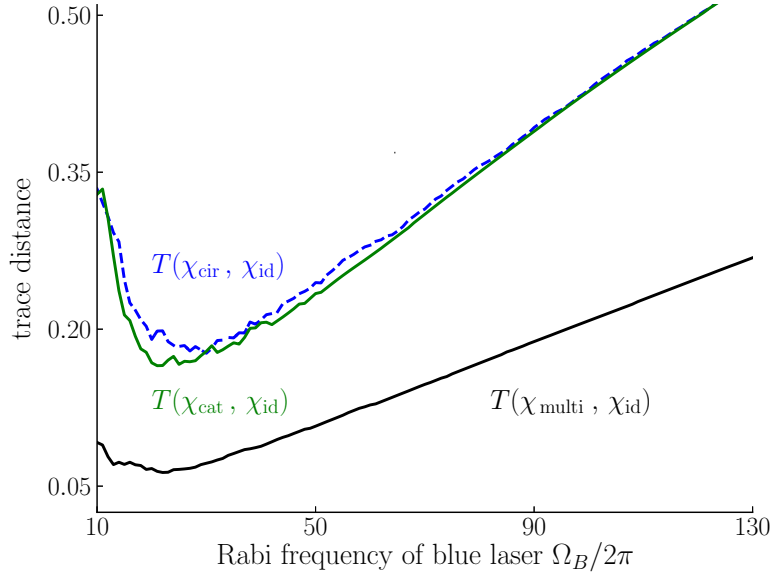


Figure 5.4.1: Trace distance between the process matrix χ_{id} for the ideal Toffoli gate and the process matrices for Rydberg interaction implementations subject to dissipation and decoherence. The results are shown as a function of the Rabi frequency Ω_B of the $|p\rangle \rightarrow |r\rangle$ (blue) laser coupling. The dashed curve is obtained by simulating all three qubits as they evolve under the sequence of gates in the Toffoli circuit, shown in Fig. 5.2.2(a). The top solid curve uses concatenation of the one- and two-qubit process matrices to compute the Toffoli circuit process matrix. The bottom (solid) curve results from simulating the multi-qubit implementation shown in Fig. 5.4.2. In all calculations 500 Monte Carlo trajectories were used with the parameters listed in Table 4.3.1.

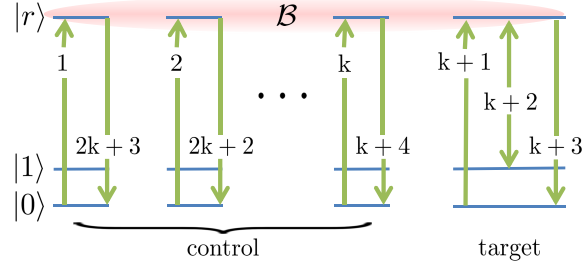


Figure 5.4.2: Multi-qubit Rydberg blockade implementation of a C_k NOT gate. Each control atom is sequentially excited from $|0\rangle$ to $|r\rangle$ in k π -pulses. Next, the target atom qubit states are swapped as in Fig 5.3.1(b), via the Rydberg state $|r\rangle$ (conditioned on no control atom populating the state $|r\rangle$). The control atoms are then returned to their original state in reverse order. The trace distance between the process matrix using this implementation for $k = 2$ and the ideal Toffoli gate is shown as the lower curve in Fig. 5.4.1.

5.5 CONCLUSION

In conclusion, we have presented an efficient method to compute the accumulation of errors in quantum circuits comprised of several few-qubit gates. Assuming the independence of errors over time and qubit register location we have shown that a set of concatenation rules on the appropriate few-qubit gate process matrices is enough to reproduce the process matrix of the entire circuit. To demonstrate the method's efficiency at calculating process matrices of large systems we considered the three-qubit Toffoli gate. The Toffoli gate may be implemented as a circuit of one- and two-qubit gates and simulations show that the process matrix obtained via concatenation is in good agreement with the result achieved by propagation through the entire circuit.

Our theory allows comparison between different implementations of gates. In particular, we compared a multi-qubit implementation of the Toffli gate with its one- and two-qubit circuit implementation. For the parameters chosen, the factor determining gate fidelity was the number of laser π -pulses. More gates lead to a lower fidelity, with a dependence that is almost linear. In this way, our analysis provides the necessary information to choose between different gate implementa-

tions. A theory of full error correction may benefit significantly from knowledge of the precise nature of errors incurred, potentially leading to higher thresholds for errors that can be remedied by appropriate error correction. The full process matrix, which remains at our disposal, may be further applied to optimally combine the Toffli gate with previous and subsequent gate operations along the lines of NMR composite pulses [101].

6

Conclusion and future development

Computation depends on performing operations to a high degree of accuracy so that we can trust the results. In quantum computation this becomes problematic as there is no direct way to observe a state of the system without disturbing it. Quantum process tomography addresses this problem through a series of measurements on states at the output of the operation. All available information about the operation can then be found in a “process matrix”. In chapter 4 we presented a numerically efficient method to obtain the process matrix for an arbitrary quantum process from a solution to the system’s master equation. The Monte Carlo wave function method on an entangled principal-ancilla system was utilized as it allows, in principal, characterisation of systems with up to 8 atoms with current computing resources. A study of the wave function trajectories also revealed that, in the case of little dissipation, a single “no-jump” wave function trajectory provided a satisfactory upper bound on the trace distance between a process matrix

simulated with decoherence and an ideal calculation.

The process matrix holds much information about the process and reducing it to a single number, e.g. using the trace distance measure, does not take full advantage of a complicated calculation. The problem is extracting meaningful information from the process matrix, a figure showing the values of the matrix elements is not enough. Therefore, a closer look at what effect the process has on individual states is required, with the intent not to find optimal experimental parameters overall but what errors afflict the low-fidelity states, and discovering methods to correct them. This may include the use of error correcting qubits or time-dependent laser pulses.

The efficiency of process characterisation with Monte Carlo wave functions was demonstrated in chapter 5 by studying the accumulation of error in a quantum circuit. This was exemplified using the three-qubit Toffoli gate which has a multi-qubit and circuit implementation. We showed that obtaining the Toffoli circuit's χ -matrix involved either a simulation or an appropriate concatenation of the one- and two-qubit gates comprising the circuit. It was found the two methods were in good agreement, but that use of the concatenation rules allowed better efficiency. The multi-qubit implementation of the Toffoli gate was facilitated by neutral atoms with Rydberg-Rydberg interactions. The fidelity of an implementation of the Toffoli gate was determined to be proportional to the number of laser π -pulses needed to perform it. More pulses led to lower fidelities.

The code developed in this thesis has been optimised for efficiency and may be easily modified to study the exact dynamics of up to 16 four-level Rydberg atoms in the presence of decoherence. This could prove useful to compare theoretical predictions with experiments involving few atom ensembles [104]. A straightforward generalization of the code could use time-dependent Rabi fields to allow, for example, the study of deterministic excitation of singly excited Rydberg states in Poisson distributed Rydberg ensembles with averages around 6-10 atoms [105].

References

- [1] D. Deutsch, “Quantum theory, the Church-Turing principle and the universal quantum computer,” *Proc. R. Soc. Lond. A* **400**, 97 (1985).
- [2] R. P. Feynman, “Simulating physics with computers,” *Int. J. Theor. Phys.* **21**, 467 (1982).
- [3] P. W. Shor, “Algorithms for quantum computation: discrete logarithms and factoring,” *Found. Com. Sc.*, 124 (1994).
- [4] P. W. Shor, “Polynomial-time algorithms for prime factorization and discrete logarithms on a quantum computer,” *SIAM J. Comput.* **26**, 1484 (1997).
- [5] M. Van den Nest, “Universal quantum computation with little entanglement,” *Phys. Rev. Lett.* **110**, 060504 (2013).
- [6] C. H. Bennet, “Logical reversibility of computation,” *J. Res. Dev.* **17**, 525 (1973).
- [7] R. Landauer, “Irreversibility and heat generation in the computing process,” *J. Res. Dev.* **5**, 183 (1961).
- [8] T. Toffoli, “Reversible computing,” in *Automata, Languages and Programming*, Lect. Comp. Sci., Vol. 85, edited by J. Bakker and J. Leeuwen (Springer, Berlin Heidelberg, 1980) pp. 632–644.
- [9] M. Mosca, “Quantum algorithms,” arXiv (2008), 0808.0369v1 .
- [10] A. K. Lenstra, H. W. Lenstra, M. S. Manasse, and J. M. Pollard, “The number field sieve,” *Proc. 22nd Ann. ACM Sym.*, 564 (1990).
- [11] R. L. Rivest, A. Shamir, and L. Adleman, “A method for obtaining digital signatures and public-key cryptosystems,” *Commun. ACM* **21**, 120 (1978).

- [12] D. Deutsch and R. Jozsa, “Rapid solution of problems by quantum computation,” *Proc. R. Soc. Lond. A* **439**, 553 (1992).
- [13] D. R. Simon, “On the power of quantum computation,” *35th Ann. Sym. Found. Com. Sci.*, 116 (1994).
- [14] L. K. Grover, “Quantum mechanics helps in searching for a needle in a haystack,” *Phys. Rev. Lett.* **79**, 325 (1997).
- [15] S. Lloyd, “Universal quantum simulators,” *Science* **273**, 1073 (1996).
- [16] C. Zalka, “Simulating quantum systems on a quantum computer,” *Proc. R. Soc. Lond. A* **454**, 313 (1998).
- [17] D. P. DiVincenzo, “The physical implementation of quantum computation,” *Fortschr. Phys.* **48**, 771 (2000).
- [18] J. I. Cirac and P. Zoller, “Quantum computations with cold trapped ions,” *Phys. Rev. Lett.* **74**, 4091 (1995).
- [19] C. Monroe, D. M. Meekhof, B. E. King, W. M. Itano, and D. J. Wineland, “Demonstration of a fundamental quantum logic gate,” *Phys. Rev. Lett.* **75**, 4714 (1995).
- [20] J. I. Cirac and P. Zoller, “A scalable quantum computer with ions in an array of microtraps,” *Nature* **404**, 579 (2000).
- [21] D. Jaksch, H.-J. Briegel, J. I. Cirac, C. W. Gardiner, and P. Zoller, “Entanglement of atoms via cold controlled collisions,” *Phys. Rev. Lett.* **82**, 1975 (1999).
- [22] G. K. Brennen, C. M. Caves, P. S. Jessen, and I. H. Deutsch, “Quantum logic gates in optical lattices,” *Phys. Rev. Lett.* **82**, 1060 (1999).
- [23] T. Calarco, E. A. Hinds, D. Jaksch, J. Schmiedmayer, J. I. Cirac, and P. Zoller, “Quantum gates with neutral atoms: Controlling collisional interactions in time-dependent traps,” *Phys. Rev. A* **61**, 022304 (2000).
- [24] D. G. Cory, A. F. Fahmy, and T. F. Havel, “Ensemble quantum computing by NMR spectroscopy,” *Proc. Nat. Acad. Sci.* **94**, 1634 (1997).
- [25] N. A. Gershenfeld and I. L. Chuang, “Bulk spin-resonance quantum computation,” *Science* **275**, 350 (1997).

- [26] R. Hanson, L. P. Kouwenhoven, J. R. Petta, S. Tarucha, and L. M. K. Vandersypen, “Spins in few-electron quantum dots,” *Rev. Mod. Phys.* **79**, 1217 (2007).
- [27] T. D. Ladd, F. Jelezko, R. Laflamme, Y. Nakamura, C. Monroe, and J. L. O’Brien, “Quantum computers,” *Nature* **464**, 45 (2010).
- [28] A. R. Calderbank and P. W. Shor, “Good quantum error-correcting codes exist,” *Phys. Rev. A* **54**, 1098 (1996).
- [29] A. M. Steane, “Error correcting codes in quantum theory,” *Phys. Rev. Lett.* **77**, 793 (1996).
- [30] M. Paris and J. Rehacek, eds., *Quantum State Estimation*, 1st ed., Lect. Not. Phys., Vol. 649 (Springer, Berlin, 2004).
- [31] A. M. Childs, I. L. Chuang, and D. W. Leung, “Realization of quantum process tomography in NMR,” *Phys. Rev. A* **64**, 012314 (2001).
- [32] N. Boulant, T. F. Havel, M. A. Pravia, and D. G. Cory, “Robust method for estimating the Lindblad operators of a dissipative quantum process from measurements of the density operator at multiple time points,” *Phys. Rev. A* **67**, 042322 (2003).
- [33] M. W. Mitchell, C. W. Ellenor, S. Schneider, and A. M. Steinberg, “Diagnosis, prescription, and prognosis of a Bell-state filter by quantum process tomography,” *Phys. Rev. Lett.* **91**, 120402 (2003).
- [34] J. L. O’Brien, G. J. Pryde, A. Gilchrist, D. F. V. James, N. K. Langford, T. C. Ralph, and A. G. White, “Quantum process tomography of a controlled-NOT gate,” *Phys. Rev. Lett.* **93**, 080502 (2004).
- [35] S. H. Myrskog, J. K. Fox, M. W. Mitchell, and A. M. Steinberg, “Quantum process tomography on vibrational states of atoms in an optical lattice,” *Phys. Rev. A* **72**, 013615 (2005).
- [36] M. Nielsen and I. Chuang, *Quantum computation and quantum information* (Cambridge university press, 2010).
- [37] I. L. Chuang and M. A. Nielsen, “Prescription for experimental determination of the dynamics of a quantum black box,” *J. Mod. Opt.* **44**, 24552467 (1997).

- [38] J. F. Poyatos, J. I. Cirac, and P. Zoller, “Complete characterization of a quantum process: The two-bit quantum gate,” *Phys. Rev. Lett.* **78**, 390 (1997).
- [39] D. W. Leung, “Choi’s proof as a recipe for quantum process tomography,” *J. Mat. Phys.* **44**, 528 (2003).
- [40] G. M. D’Ariano and P. Lo Presti, “Quantum tomography for measuring experimentally the matrix elements of an arbitrary quantum operation,” *Phys. Rev. Lett.* **86**, 4195 (2001).
- [41] J. B. Altepeter, D. Branning, E. Jeffrey, T. C. Wei, P. G. Kwiat, R. T. Thew, J. L. O’Brien, M. A. Nielsen, and A. G. White, “Ancilla-assisted quantum process tomography,” *Phys. Rev. Lett.* **90**, 193601 (2003).
- [42] G. M. D’Ariano and P. Lo Presti, “Imprinting complete information about a quantum channel on its output state,” *Phys. Rev. Lett.* **91**, 047902 (2003).
- [43] M. Mohseni and D. A. Lidar, “Direct characterization of quantum dynamics,” *Phys. Rev. Lett.* **97**, 170501 (2006).
- [44] M. Mohseni and D. A. Lidar, “Direct characterization of quantum dynamics: General theory,” *Phys. Rev. A* **75**, 062331 (2007).
- [45] Z.-W. Wang, Y.-S. Zhang, Y.-F. Huang, X.-F. Ren, and G.-C. Guo, “Experimental realization of direct characterization of quantum dynamics,” *Phys. Rev. A* **75**, 044304 (2007).
- [46] M. Mohseni, A. T. Rezakhani, and D. A. Lidar, “Quantum-process tomography: Resource analysis of different strategies,” *Phys. Rev. A* **77**, 032322 (2008).
- [47] C. Gardiner and P. Zoller, *Quantum noise: a handbook of Markovian and non-Markovian quantum stochastic methods with applications to quantum optics* (Springer, 2004).
- [48] J. Dalibard, Y. Castin, and K. Mølmer, “Wave-function approach to dissipative processes in quantum optics,” *Phys. Rev. Lett.* **68**, 580 (1992).
- [49] K. Mølmer, Y. Castin, and J. Dalibard, “Monte Carlo wave-function method in quantum optics,” *J. Opt. Soc. Am. B* **10**, 524 (1993).

- [50] R. Dum, P. Zoller, and H. Ritsch, “Monte Carlo simulation of the atomic master equation for spontaneous emission,” *Phys. Rev. A* **45**, 4879 (1992).
- [51] F. Bardou, J. P. Bouchaud, O. Emile, A. Aspect, and C. Cohen-Tannoudji, “Subrecoil laser cooling and lévy flights,” *Phys. Rev. Lett.* **72**, 203 (1994).
- [52] J. C. Butcher, *Numerical methods for ordinary differential equations* (John Wiley, 2003).
- [53] F. Reiter and A. S. Sørensen, “Effective operator formalism for open quantum systems,” *Phys. Rev. A* **85**, 032111 (2012).
- [54] O. Gamel and D. F. V. James, “Time-averaged quantum dynamics and the validity of the effective hamiltonian model,” *Phys. Rev. A* **82**, 052106 (2010).
- [55] H. Feshbach, “Unified theory of nuclear reactions,” *Ann. Phys.* **5**, 357390 (1958).
- [56] I. Rotter, “A non-Hermitian Hamilton operator and the physics of open quantum systems,” *J. Phys. A* **42**, 153001 (2009).
- [57] K. Kraus, A. Böhm, J. Dollard, and W. Wootters, “States, effects, and operations fundamental notions of quantum theory,” (Springer Berlin Heidelberg, 1983).
- [58] D. J. Wineland, C. Monroe, W. M. Itano, D. Leibfried, B. E. King, and D. M. Meekhof, “Experimental issues in coherent quantum-state manipulation of trapped atomic ions,” *J. Res. Nat. Inst. Stand. Tech.* **103**, 259328 (1998).
- [59] F. Schmidt-Kaler, H. Häffner, M. Riebe, S. Gulde, G. P. Lancaster, T. Deuschle, C. Becher, C. F. Roos, J. Eschner, and R. Blatt, “Realization of the Cirac–Zoller controlled-NOT quantum gate,” *Nature* **422**, 408 (2003).
- [60] T. Monz, K. Kim, W. Hänsel, M. Riebe, A. S. Villar, P. Schindler, M. Chwalla, M. Hennrich, and R. Blatt, “Realization of the quantum Toffoli gate with trapped ions,” *Phys. Rev. Lett.* **102**, 040501 (2009).
- [61] I. Bloch, “Quantum coherence and entanglement with ultracold atoms in optical lattices,” *Nature* **453**, 1016 (2008).
- [62] I. H. Deutsch, G. K. Brennen, and P. S. Jessen, “Quantum computing with neutral atoms in an optical lattice,” *Fortsch. Phys.* **48**, 925943 (2000).

- [63] D. Jaksch, J. I. Cirac, P. Zoller, S. L. Rolston, R. Côté, and M. D. Lukin, “Fast quantum gates for neutral atoms,” *Phys. Rev. Lett.* **85**, 2208 (2000).
- [64] Z. Hu and H. J. Kimble, “Observation of a single atom in a magneto-optical trap,” *Opt. Lett.* **19**, 1888 (1994).
- [65] J. D. Miller, R. A. Cline, and D. J. Heinzen, “Far-off-resonance optical trapping of atoms,” *Phys. Rev. A* **47**, R4567 (1993).
- [66] M. Greiner, O. Mandel, T. Esslinger, T. W. Hänsch, and I. Bloch, “Quantum phase transition from a superfluid to a Mott insulator in a gas of ultracold atoms,” *Nature* **415**, 39 (2002).
- [67] R. Dumke, M. Volk, T. Mütter, F. B. J. Buchkremer, G. Birkl, and W. Ertmer, “Micro-optical realization of arrays of selectively addressable dipole traps: A scalable configuration for quantum computation with atomic qubits,” *Phys. Rev. Lett.* **89**, 097903 (2002).
- [68] M. Saffman and T. G. Walker, “Creating single-atom and single-photon sources from entangled atomic ensembles,” *Phys. Rev. A* **66**, 065403 (2002).
- [69] P. Rabl, A. J. Daley, P. O. Fedichev, J. I. Cirac, and P. Zoller, “Defect-suppressed atomic crystals in an optical lattice,” *Phys. Rev. Lett.* **91**, 110403 (2003).
- [70] S. Peil, J. V. Porto, B. L. Tolra, J. M. Obrecht, B. E. King, M. Subbotin, S. L. Rolston, and W. D. Phillips, “Patterned loading of a Bose-Einstein condensate into an optical lattice,” *Phys. Rev. A* **67**, 051603 (2003).
- [71] M. Saffman, “Addressing atoms in optical lattices with Bessel beams,” *Opt. Lett.* **29**, 1016 (2004).
- [72] J. Vala, A. V. Thapliyal, S. Myrgren, U. Vazirani, D. S. Weiss, and K. B. Whaley, “Perfect pattern formation of neutral atoms in an addressable optical lattice,” *Phys. Rev. A* **71**, 032324 (2005).
- [73] M. Saffman and T. G. Walker, “Analysis of a quantum logic device based on dipole-dipole interactions of optically trapped Rydberg atoms,” *Phys. Rev. A* **72**, 022347 (2005).

- [74] M. Saffman, T. G. Walker, and K. Mølmer, “Quantum information with Rydberg atoms,” *Rev. Mod. Phys.* **82**, 2313 (2010).
- [75] C. Zhang, S. L. Rolston, and S. Das Sarma, “Manipulation of single neutral atoms in optical lattices,” *Phys. Rev. A* **74**, 042316 (2006).
- [76] D. D. Yavuz, P. B. Kulatunga, E. Urban, T. A. Johnson, N. Proite, T. Henage, T. G. Walker, and M. Saffman, “Fast ground state manipulation of neutral atoms in microscopic optical traps,” *Phys. Rev. Lett.* **96**, 063001 (2006).
- [77] Y. O. Dudin and A. Kuzmich, “Strongly interacting Rydberg excitations of a cold atomic gas,” *Science* **336**, 887 (2012).
- [78] V. Bendkowsky, B. Butscher, J. Nipper, J. P. Shaffer, R. Löw, and T. Pfau, “Observation of ultralong-range Rydberg molecules,” *Nature* **458**, 1005 (2009).
- [79] M. Saffman and T. G. Walker, “Entangling single- and n -atom qubits for fast quantum state detection and transmission,” *Phys. Rev. A* **72**, 042302 (2005).
- [80] E. Brion, K. Mølmer, and M. Saffman, “Quantum computing with collective ensembles of multilevel systems,” *Phys. Rev. Lett.* **99**, 260501 (2007).
- [81] T. G. Walker and M. Saffman, “Consequences of Zeeman degeneracy for the van der Waals blockade between Rydberg atoms,” *Phys. Rev. A* **77**, 032723 (2008).
- [82] I. I. Ryabtsev, D. B. Tretyakov, and I. I. Beterov, “Applicability of Rydberg atoms to quantum computers,” *J. Phys. B* **38**, S421 (2005).
- [83] D. Tong, S. M. Farooqi, J. Stanojevic, S. Krishnan, Y. P. Zhang, R. Côté, E. E. Eyler, and P. L. Gould, “Local blockade of Rydberg excitation in an ultracold gas,” *Phys. Rev. Lett.* **93**, 063001 (2004).
- [84] T. C. Liebisch, A. Reinhard, P. R. Berman, and G. Raithel, “Atom counting statistics in ensembles of interacting Rydberg atoms,” *Phys. Rev. Lett.* **95**, 253002 (2005).
- [85] T. Vogt, M. Viteau, J. Zhao, A. Chotia, D. Comparat, and P. Pillet, “Dipole blockade at Föster resonances in high resolution laser excitation of Rydberg states of cesium atoms,” *Phys. Rev. Lett.* **97**, 083003 (2006).

- [86] L. Isenhower, M. Saffman, and K. Mølmer, “Multibit C_k NOT quantum gates via Rydberg blockade,” *Quant. Inf. Proc.* **10**, 755770 (2011).
- [87] M. D. Lukin, M. Fleischhauer, R. Cote, L. M. Duan, D. Jaksch, J. I. Cirac, and P. Zoller, “Dipole blockade and quantum information processing in mesoscopic atomic ensembles,” *Phys. Rev. Lett.* **87**, 037901 (2001).
- [88] M. Saffman and K. Mølmer, “Scaling the neutral-atom rydberg gate quantum computer by collective encoding in holmium atoms,” *Phys. Rev. A* **78**, 012336 (2008).
- [89] E. Urban, T. Johnson, T. Henage, L. Isenhower, D. Yavuz, T. Walker, and M. Saffman, “Observation of Rydberg blockade between two atoms,” *Nat. Phys.* **5**, 110 (2009).
- [90] Y. Miroshnychenko, A. Gaëtan, C. Evellin, P. Grangier, D. Comparat, P. Pillet, T. Wilk, and A. Browaeys, “Coherent excitation of a single atom to a Rydberg state,” *Phys. Rev. A* **82**, 013405 (2010).
- [91] T. A. Johnson, E. Urban, T. Henage, L. Isenhower, D. D. Yavuz, T. G. Walker, and M. Saffman, “Rabi oscillations between ground and Rydberg states with dipole-dipole atomic interactions,” *Phys. Rev. Lett.* **100**, 113003 (2008).
- [92] C. Gerry and P. Knight, *Introductory quantum optics* (Cambridge university press, 2005).
- [93] E. Brion, L. H. Pedersen, and K. Mølmer, “Adiabatic elimination in a lambda system,” *J. Phys. A: Mathematical and Theoretical* **40**, 1033 (2007).
- [94] X. L. Zhang, A. T. Gill, L. Isenhower, T. G. Walker, and M. Saffman, “Fidelity of a Rydberg-blockade quantum gate from simulated quantum process tomography,” *Phys. Rev. A* **85**, 042310 (2012).
- [95] Y. S. Weinstein, T. F. Havel, J. Emerson, N. Boulant, M. Saraceno, S. Lloyd, and D. G. Cory, “Quantum process tomography of the quantum Fourier transform,” *J. Chem. Phys.* **121**, 6117 (2004).
- [96] H. Carmichael, *An open systems approach to Quantum Optics*, Vol. 18 (Springer, 1993).

- [97] M. Saffman, X. Zhang, A. Gill, L. Isenhower, and T. Walker, “Rydberg state mediated quantum gates and entanglement of pairs of neutral atoms,” *J. Phys. Conf. Ser.* **264**, 012023 (2011).
- [98] Y. Castin and K. Mølmer, “Monte Carlo wave functions and nonlinear master equations,” *Phys. Rev. A* **54**, 5275 (1996).
- [99] A. Steane, “Multiple-particle interference and quantum error correction,” *Proc. R. Soc. Lond. A* **452**, 2551 (1996).
- [100] L. Viola and S. Lloyd, “Dynamical suppression of decoherence in two-state quantum systems,” *Phys. Rev. A* **58**, 2733 (1998).
- [101] M. H. Levitt, “Composite pulses,” *Prog. Nucl. Magn. Reson. Spect.* **18**, 61 (1986).
- [102] J. A. Jones, “Designing short robust NOT gates for quantum computation,” *Phys. Rev. A* **87**, 052317 (2013).
- [103] K. Mølmer, L. Isenhower, and M. Saffman, “Efficient Grover search with Rydberg blockade,” *J. Phys. B* **44**, 184016 (2011).
- [104] M. Ebert, A. Gill, M. Gibbons, X. Zhang, M. Saffman, and T. G. Walker, “Atomic fock state preparation using Rydberg blockade,” *Phys. Rev. Lett.* **112**, 043602 (2014).
- [105] D. Petrosyan and K. Mølmer, “Stimulated adiabatic passage in a dissipative ensemble of atoms with strong Rydberg-state interactions,” *Phys. Rev. A* **87**, 033416 (2013).

ENGLISH SUMMARY

Quantum computation has opened up a new way to think about computation by utilizing physical systems that display features unique to quantum mechanics. These features have been harnessed to create algorithms that promise exponential speed-up over classical equivalents. This thesis presents efficient methods for characterizing quantum processes and, more specifically, how that applies to characterizing the gates used in quantum computation. We discuss neutral atoms as a promising route to large scale quantum computing and construct a numerical model to simulate this system efficiently. Neutral Rydberg atoms and their interactions have been exploited for fast multi-atom quantum gates and we show how our method can aid these experiments to achieve optimal results.

DANISH SUMMARY

Udviklingen af kvantecomputere har resulteret i en helt ny måde at tænke på informationsbehandling, hvor man udnytter kvanteegenskaber ved fysiske systemer, som ikke har nogen klassisk ækvivalens. Disse egenskaber er blevet brugt til at skabe kvantealgoritmer, der er eksponentielt hurtigere end deres klassiske modstykker. Denne afhandling analyserer effektive metoder til at karakterisere kvanteprocessor og mere specifikt, hvordan de kan bruges til at karakterisere de såkaldte kvante-gates. Vi beskriver, hvorledes kolde atomer er et lovende system til at realisere kvanteberegninger på stor skala, og vi konstruerer en effektiv metode til at simulere disse systemer numerisk. Hurtige multiatom kvante-gates er blevet konstrueret med neutrale Rydberg atomer, og vi viser, hvordan vores metode kan hjælpe disse eksperimenter med at opnå optimale resultater.